Title
APPLICATIONS OF TIME-DIFFERENTIAL PERTURBED ANGULAR CORRELATIONS TO THE STUDY OF SOLIDS

Author
Schwartz, Gary Paul.

Publication Date
1975-06-01

LBL-4056
c.1

APPLICATIONS OF TIME-DIFFERENTIAL PERTURBED ANGULAR CORRELATIONS TO THE STUDY OF SOLIDS

Gary Paul Schwartz
(Ph. D. thesis)

June 1975

Prepared for the U. S. Energy Research and Development Administration under Contract W-7405-ENG-48

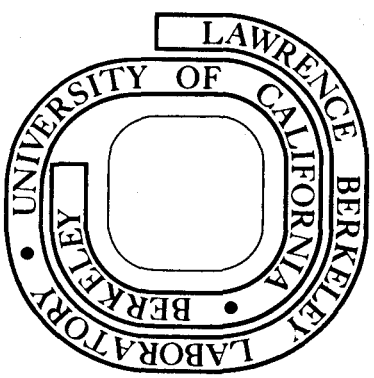

LBL-4056
c.1

DISCLAIMER

Rem tene; verba sequentur.

Cato, The Elder

Grasp the subject, the words will follow.

TABLE OF CONTENTS

APPLICATIONS OF TIME-DIFFERENTIAL PERTURBED ANGULAR CORRELATIONS TO THE STUDY OF SOLIDS

Gary Paul Schwartz

(Ph. D. Thesis)

Department of Chemistry, and Lawrence Berkeley Laboratory
University of California, Berkeley, California 94720

April 1975

ABSTRACT

Time-differential perturbed angular correlation techniques were applied to a systematic study of insulating antiferromagnets and rare-earth intermetallic alloys doped with either ^{111m}Cd or ^{111}In. The internal magnetic fields and electric field gradients at the radioactive nucleus are deduced from the experimentally measured perturbation factors. The analysis of fluoride, chloride, oxide, and sulfide data shows the systematic variation of the observed supertransferred hyperfine fields with the intervening anion covalency and allows one to extract covalency parameters after the adoption of a simple model. A comparison of the transferred hyperfine field data between fluoride perovskites and the corresponding quadratic layer compounds produces a value for the zero-point spin deviation in magnetically two-dimensional antiferromagnets which is in qualitative agreement with existing theoretical estimates. Paramagnetic shifts due to transferred hyperfine field and field-induced spin-flopping have also been observed. By careful temperature regulation we have been able to plot out the temperature dependence of the sublattice magnetization next to a diamagnetic impurity in $RbMnF_3$ and MnF_2. A shift in the

transferred hyperfine field at Cd doped into MnS has been measured under the application of moderate pressures up to 22 kbar. Analysis of the electric field gradients at the In and Sn sites in the rare-earth series RIn_3 and RSn_3 as functions of temperature and pressure has permitted us to check for valence fluctuations in certain of these alloys.

I. INTRODUCTION

The early 20th century saw the advent of the directed valence bond proposals of Pauling[1] and its associated concept of covalent bonding between atoms. It was not known to what degree the idea of covalent bonding could be applied to salts containing strongly electronegative anions, and Van Vleck[2] had developed a relatively successful model to explain the magnetic properties of a number of transition metal salts based on a purely "ionic" crystal field analysis. The postwar application of the new resonance techniques (NMR, EPR, ENDOR) to these materials, previously considered to be purely ionic, was to prove a testing ground for the general applicability of the covalency concept and for the further elucidation of the fundamental nature of the chemical bond.

The nature of the chemical bond was not the only problem which drew attention to the transition metal salts; concurrent theoretical advances by Kramers[3] involving the role of nonmagnetic atoms in explaining the existence of long range magnetic order had been put forth and developed subsequently by many authors. The concept of superexchange[4] associated with the change in the paramagnetic ion wave function due to admixture of symmetry allowed ligand orbitals was integrally tied to the discussion of covalency in these compounds.

The late entry of neutron diffraction, Mössbauer, and perturbed angular correlation studies into this field can be understood in terms of the experimental difficulties which must be surmounted. For PAC measurements the insulating nature of these compounds requires a nuclear cascade which proceeds via either beta decay or an isomeric transition in order to avoid multiply charged electronic states following the decay

which would wash out the correlation. The radioactive nucleus must have in addition an ionic radius and oxidation state commensurate with that of the magnetic impurity which it replaces. These stringent requirements narrow the field of available nuclei to essentially one candidate, ^{111m}Cd, with its attendant half-life of 49 minutes. Since Cd p or d orbitals can contribute to nuclear magnetic fields only through core polarization, transferred spin density into Cd s shells via the Fermi contact term will dominate the magnetic hyperfine interaction. The spherical symmetry exhibited by s shells results in a σ or s bond specific interaction, thereby providing a distinct advantage over other techniques.

It was this combination of unique bonding information available to PAC and the continued need to study concentrated magnetic systems exhibiting long range order which provided the impetus for undertaking the measurements. We thus systematically studied a large range of insulting antiferromagnets which encompassed fluorides, oxides, chlorides, and sulfides as anions. In order to make comparisons between compounds with different covalency parameters and to check the predictions of superexchange theories, we have further required the impurity to be octahedrally coordinated with only linear metal-ligand-impurity bonds.

Our interests have ranged beyond the data available from a simple chemical bond analysis; we have also used the transferred hyperfine field at the Cd nucleus in order to probe a variety of solid state phenomena. In this vein we have detected spin deviations in magnetically two-dimensional antiferromagnets due to quantum mechanical zero-point motion as well as probing the temperature dependence of the sublattice magnetization next to a diamagnetic impurity. Measurements in an applied

external field have yielded paramagnetic shifts due to transferred fields and the observation of the flipping of the magnetization axis at a critical field in $RbMnF_3$.

The quest to apply PAC to the study of physical phenomena has not been limited to utilizing transferred magnetic fields. Using the electric field gradient at the tetragonal site in the rare-earth series RIn_3 and RSn_3, we have demonstrated a high sensitivity method for discriminating between rare-earth valence states and have checked for temperature and pressure induced valence fluctuations in a number of Ce, Eu, and Yb compounds.

II. PAC FORMALISM

The exact quantum mechanical description of the angular distribution of radiations emitted from an ensemble of nuclei is based on the transformation properties of spherical tensors, the manipulations of Racah algebra, and the statistical formalism of the density matrix. I plan to forego duplicating this involved description and will pursue instead the basic physical ideas involved and will describe in a general way the results which will be pertinent to the data analysis. The reader who requires more rigor will find that the literature[5,6,7] fairly abounds in comprehensive tracts which include all of the formal details of the theory.

Our basic picture centers around a statistical ensemble of nuclei which will emit radiation isotropically if they have no preferred direction in space. We wish to explain in physical terms how this ensemble is prepared so that the associated nuclear angular momenta are preferentially oriented with the result that the emitted radiation will in general be anisotropic.

If one considers a deexcitation taking place between two nuclear levels with angular momentum I_i and I_f with projection quantum numbers M_i and M_f, then the quantum mechanical description of the radiated angular momentum of a photon field contains in it the selection rules for allowed multipole transitions between quantum states. A photon carrying $\hbar\ell$ units of angular momentum with projection quantum number m connects the initial and final states such that

$$\begin{aligned} |I_i - I_f| \leq \ell \leq |I_i + I_f| \\ m = M_i - M_f. \end{aligned} \tag{1}$$

In principal the emitted radiation will contain all the multipole character consistent with the allowed values of ℓ, but in practice the transition probabilities are scaled by a factor of order $(a/\lambda)^{2\ell}$, where a and λ are parameters characteristic of the nuclear diameter and the wavelength of the emitted radiation. For the actual cascades (Fig. 1) which were used in this work, the radiations are essentially unmixed and carry away the minimum allowed angular momentum. By performing a measurement which detects the emitted photon, we select out of space a quantization axis with respect to the ensemble of nuclei. In the simplest case (ℓ = 1, dipole radiation), the projection of the photons angular momentum along the quantization axis is m = ± 1. In this case the state m = 0 is not allowed since a transverse field cannot carry angular momentum along its direction of propagation. Inspection of the selection rules (Eq. 1) for the allowed transitions shows that certain transitions are now forbidden and thus the final state subpopulations associated with the M_f quantum numbers will be unequal. An equivalent statement is that the final state now shows a preferential direction in space specified by the quantization axis, and subsequent photon emission from this state will not be generally isotropic.

A. The Unperturbed Directional Correlation Function

The techniques of Racah algebra and the density matrix formalism for handling an ensemble of statistical spins can be used to quantify the simple picture of a two-photon cascade and the emission anisotropy of the second radiation. It is a general result[8] of the angular momentum properties of a photon field that the directional correlation function for a γ_1-γ_2 cascade can be written as

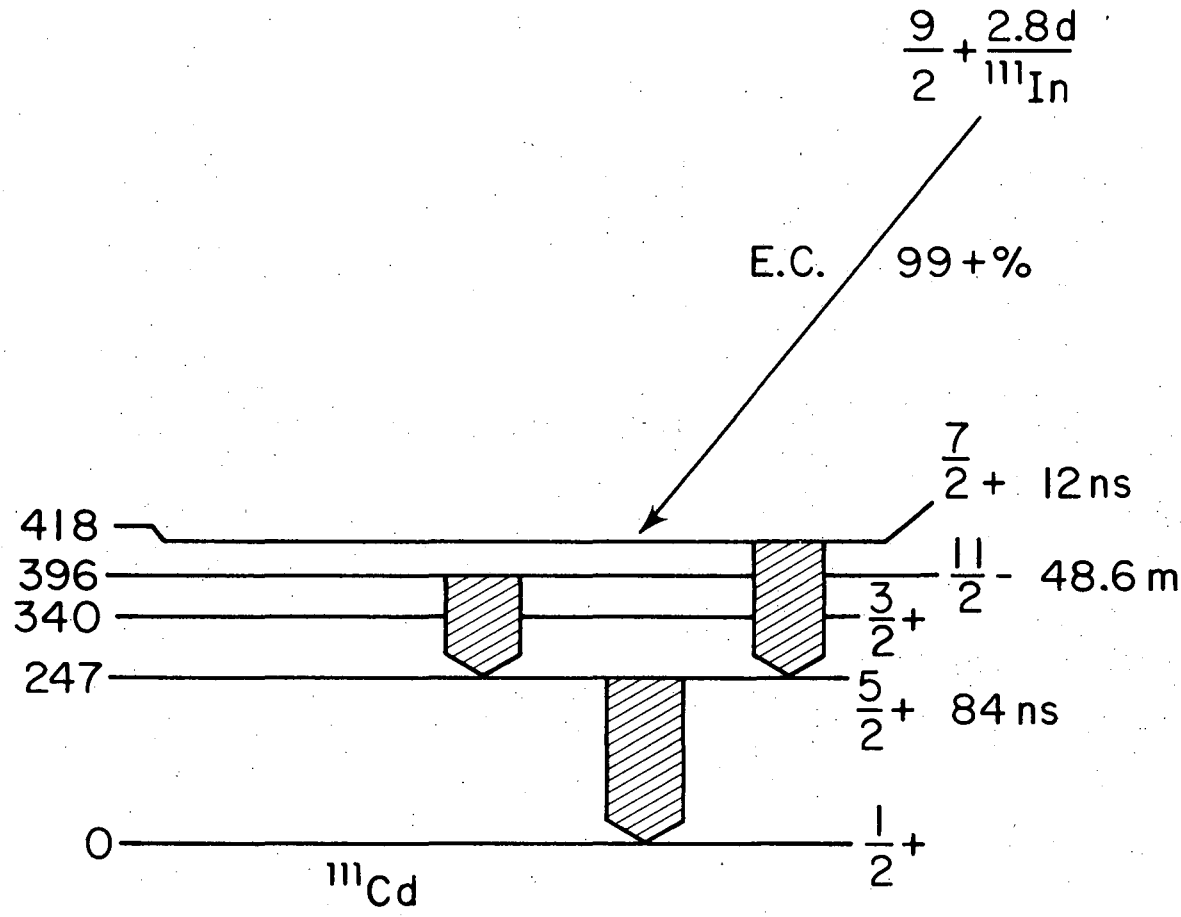

$^{111}In \xrightarrow[\gamma\text{-}\gamma]{E.C.} {}^{111}Cd \quad \left(\frac{7}{2}+ \rightarrow \frac{5}{2}+ \rightarrow \frac{1}{2}+\right)$

$^{111m}Cd \xrightarrow{\gamma\text{-}\gamma} {}^{111}Cd \quad \left(\frac{11}{2}- \rightarrow \frac{5}{2}+ \rightarrow \frac{1}{2}+\right)$

XBL758-3699

Fig. II.1

$$W(\theta) = \sum_k A_{k_1} A_{k_2} P_k(\cos\theta) \qquad (2)$$

where k takes on only even values for photon-photon correlations and obtains a maximum cutoff value of 2I, $2\ell_1$, or $2\ell_2$, whichever is smallest. Here I is the intermediate level spin and ℓ_1 and ℓ_2 are the multipolarities of the radiation for the first and second photons. The $P_k(\cos\theta)$ are the Legendre polynomials, and for pure multipole radiation the A_k's are functions of the multipole order and the initial and final spins of the states connected by the transition. For purposes of the ^{111m}Cd and ^{111}In cascades (Fig. 1), k can be effectively truncated at 2 and the normalized unperturbed correlation function written as:

$$W(\theta) = 1 + A_{22}P_2(\cos\theta), \text{ where } A_{22} \equiv A_{k_1}A_{k_2} \text{ for } k = 2. \qquad (3)$$

A_{22} for ^{111m}Cd is + 0.16, while A_{22} for ^{111}In is -0.15. The sign difference is due to the nuclear spin sequences and photon multipolarities involved in the two different decay schemes.

B. The Perturbed Directional Correlation Function for Static Interactions

A few words are in order concerning the physical meaning of a "perturbed" directional angular correlation. Directional correlations in the absence of static magnetic fields or electric field gradients will not depend on the time elapsed by the nucleus in the intermediate state. However for a nuclear state which has a non-zero spin or finite quadrupole moment, the presence of static magnetic fields or electric field gradients will cause the nuclear state to precess relative to the quantization axis defined by the perturbing field. In order for the perturbing field to be effective in causing a finite rotation of the nuclear state prior to the emission of a gamma quantum, the state must have a finite lifetime comparable to the time associated with the precession

frequency. This precession of the nuclear state prior to the emission of the second detected photon impresses a quantum beat modulation onto the observed directional correlation pattern due to time dependent repopulation shifts in the emitting state sublevels.

Under the assumption of "static" perturbing fields the time-modulated perturbed angular correlation becomes[6]

$$W(\theta,t) = \sum_{k_1 N_1} \sum_{k_2 N_2} A_{k_1} A_{k_2} \left[(2k_1+1)\ (2k_2+1)\right]^{-\frac{1}{2}}$$

$$\times\ G_{k_1 k_2}^{N_1 N_2}(t)\ Y_{k_1}^{N_1 *}(\vec{k}_1)\ Y_{k_2}^{N_2}(\vec{k}_2). \qquad (4)$$

For a polycrystalline sample one needs to integrate over all possible orientations with the constraint that the angle θ between the emission directions $\vec{k}_1$ and $\vec{k}_2$ be held fixed. Truncating the maximum k values at 2 and performing the integration yields

$$W(\theta,t) = 1 + A_{22} G_{22}(t) P_2(\cos\theta). \qquad (5)$$

The perturbation factor $G_{22}(t)$ contains all the time dependence and for static fields has the form[6]

$$G_{22}(t) = \sum_{N=-2}^{+2} \sum_{n_1,n_2} \sum_{m_1,m_2} (-1)^{2I+m_1+m_2} \exp\left(-\frac{i}{\hbar}[E_{n_1} - E_{n_2}]t\right)$$

$$\times \begin{pmatrix} I & I & 2 \\ m_1' & -m_1 & N \end{pmatrix} \begin{pmatrix} I & I & 2 \\ m_2' & -m_2 & N \end{pmatrix} \langle n_1|m_2\rangle^* \langle n_1|m_1\rangle \langle n_2|m_2'\rangle \langle n_2|m_1'\rangle^* . \qquad (6)$$

Here $|m_1\rangle$, $|m_1'\rangle$, $|m_2\rangle$, $|m_2'\rangle$ are eigenfunctions and $|n_1\rangle$, $|n_2\rangle$

eigenvectors of the Hamiltonian belonging to the eigenvalues E_{n_1} and E_{n_2} respectively. In the presence of both an internal magnetic field H_{int} and an electric field gradient eq_{zz}, the Hamiltonian describing the interaction with the nuclear spins and quadrupole moment is

$$\mathcal{H} = - \gamma \hbar \vec{H}_{int} \cdot \vec{I} + \frac{e^2 q_{zz} Q}{4I(2I-1)} \{3I_z^2 - I(I+1) + \eta (I_x^2 - I_y^2)\} . \qquad (7)$$

The components of $\vec{I}$ refer to the principal axes of the field gradient tensor. Our experiments essentially spanned the three possibilities for the Hamiltonian of Eq. 7, i.e. a pure magnetic interaction, a pure electric field gradient, and a combined interaction of the most general sort where the principal axis of the electric field gradient does not coincide with the internal magnetic field direction.

For the purely magnetic interaction involving an intermediate level of spin 5/2 the perturbation factor for a polycrystalline sample is a simple analytic function given by

$$G_{22}(t) = 1/5 \ (1 + 2 \cos \omega_L t + 2 \cos 2 \omega_L t) , \qquad (8)$$

where ω_L is the Larmor precession frequency $g\mu_N H_{int}/\hbar$.

The Hamiltonian for the pure quadrupole case is not diagonal unless the electric field gradient has axial symmetry, in which case $\eta = 0$ and the perturbation function for spin 5/2 once again has a simple analytic form

$$G_{22}(t) = \frac{1}{5} \ 1 + \frac{13}{7} \cos\omega_Q t + \frac{10}{7} \cos 2\omega_Q t + \frac{5}{7} \cos\omega 3_Q t$$

and

$$\omega_Q = 3e^2 q_{zz} Q / \hbar 2I(2I-1). \qquad (9)$$

For electric field gradients lacking axial symmetry η will not be zero and $G_{22}(t)$ must be generated numerically. This is also true of the combined interaction, for which one must diagonalize the Hamiltonian (7) in order to calculate the eigenvalues and eigenvectors needed for the evaluation of $G_{22}(t)$.

C. Applied Magnetic Fields

Certain situations dictate experiments in the paramgnetic state, i.e. $H_{int} = 0$. One can still extract data pertinent to the magnetic properties by applying a magnetic field perpendicular to the plane of the detectors. There is now one field fixed in space perpendicular to the correlation plane rather than an internal field whose axis is randomly oriented relative to the correlation plane. The perturbed correlation function for a static magnetic field H perpendicular to the plane of the detectors is given by[9]

$$W(\theta,t,H_{\perp}) = \sum_{k \text{ even}} b_k \cos k(\theta-\omega_L t). \qquad (10)$$

The same fundamental information is available from both the applied field and internal field cases, i.e. the Larmor precession frequency $\omega_L = g\mu_n H/\hbar$, but the Fourier coefficients of the perturbation factors for the two cases are now different.

III. APPARATUS

Data for this thesis were collected on two separate γ-γ coincidence spectrometers, one employing four counters and the other eight. We found it advantageous to run both spectrometers simultaneously, usually reserving the eight-counter system for those compounds which would require more statistics in the analysis, e.g. in the case of combined interactions. A given detector is used as both a START and a STOP in the eight-counter system, and it was able to accumulate data at a rate of nearly six times that of the older four-counter system.

A. The Four-Counter System Electronics

Figure 2 shows the basic schematic for the four-counter system. The detectors were 1×1½" NaI(Tl) crystals followed by Amperex 56 DVP photomultipliers and LBL designed preamps. The fast signals were clipped with a shorted delay line and fed into EG&G TD101 differential discriminators. Both START and STOP output pulses from the discriminators strobed an Ortec 437A time-to-amplitude converter (TAC), but the STOP signals were run through a passive delay box prior to entering the TAC in order to provide a time region in which only chance coincidences could be accumulated. The slow side of the preamps fed LBL designed linear amplifiers and single-channel analyzers (SCA) and the output signals were fed into a slow coincidence unit. The output of this slow coincidence unit was used to trigger a mixer-delay gate whose input was the TAC output signal, and the gate output which represented the slow-fast coincidence data was fed into a Scipp 1600 channel analyzer with appropriate routing to record two 180° and two 90° spectra. After the spectra had been accumulated on the Scipp, they were

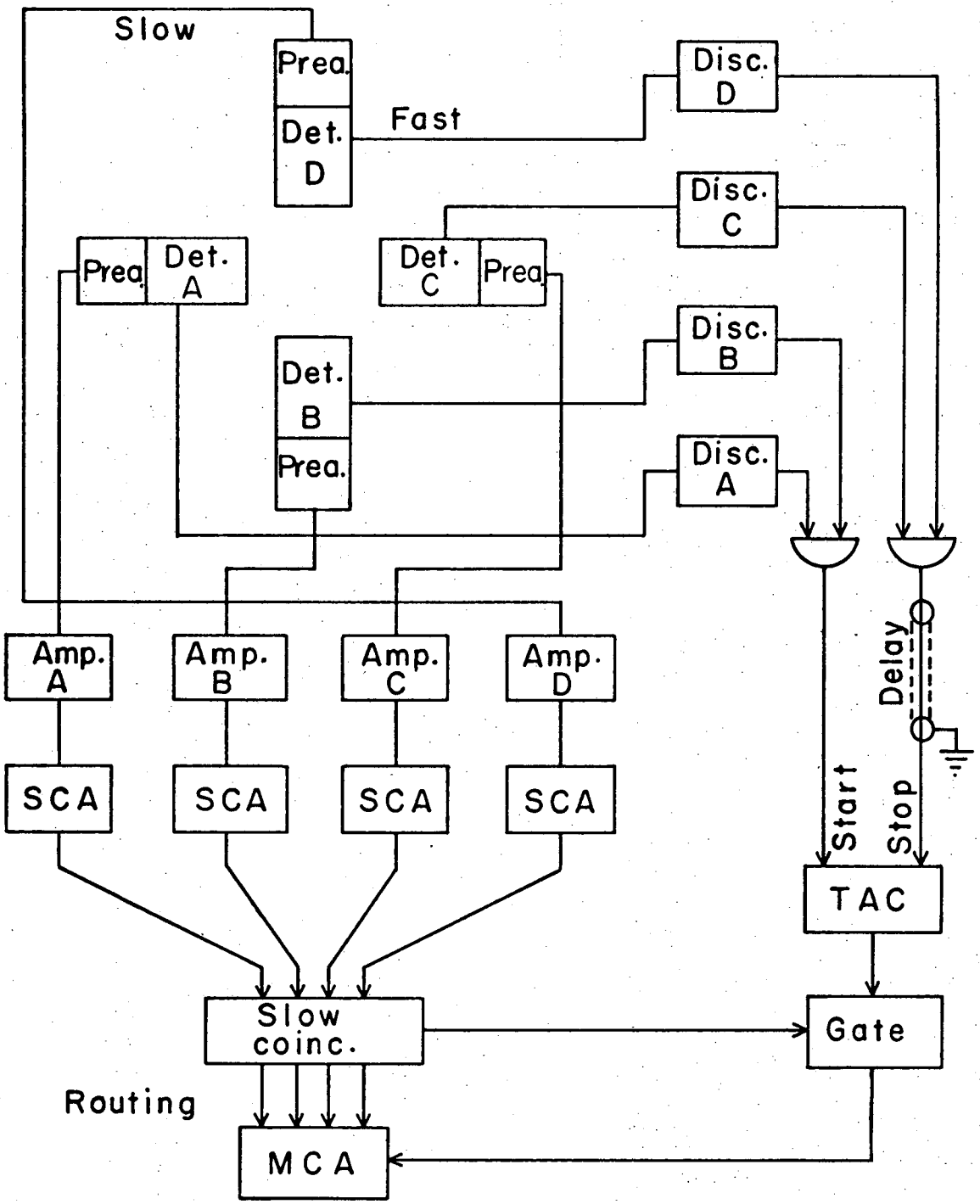

Fig. III-2.

XBL.714 - 3246

recorded on a Kennedy Incremental 1500 tape unit for subsequent analysis. The typical time resolution for this system was 1.8 ns FWHM on the ^{22}Na 511-511 cascade with the SCA windows set up for the ^{111m}Cd cascade. An Eldorado 610 Digital Delay Generator and calibrated lengths of delay cable were used to establish the time calibration.

B. The Eight-Counter System Electronics

The eight-counter system was designed to produce higher counting efficiency and better time resolution than the older system. Figure 3 shows the essential pulse sequencing for one detector. The use of two SCA's plus additional circuitry allowed each detector to be used as both a START and a STOP detector. 1×1½" NaI(Tl) scintillators were used with RCA 8850 photomultiplier tubes which had been selected for minimal gain shifts at high counting rates. The LBL preamps were modified so that the final dynodes were held at a fixed voltage by Zener diodes to further improve the high counting rate capacity of the system. The fast output of the preamps fed constant fraction discriminators of a type described by Maier and Sperr.[10] The fast pulse shaper produces outputs which feed circuits to suppress multiple coincidences as well as feeding the basic fast timing data into a high speed coincidence circuit similar to that described by Gerholm et al.[11] With this circuitry each detector functioned both as a start and a stop and triple and quadrupole coincidences were suppressed to better than 0.05% even at high counting rates. The fast coincidence data fed an LBL designed TAC whose output was directed through a delay into the input of a linear gate. The gate trigger was strobed by the slow logic and multiple coincidence suppression circuitry, and the final timing information was directed to an 8192 channel Hewlett

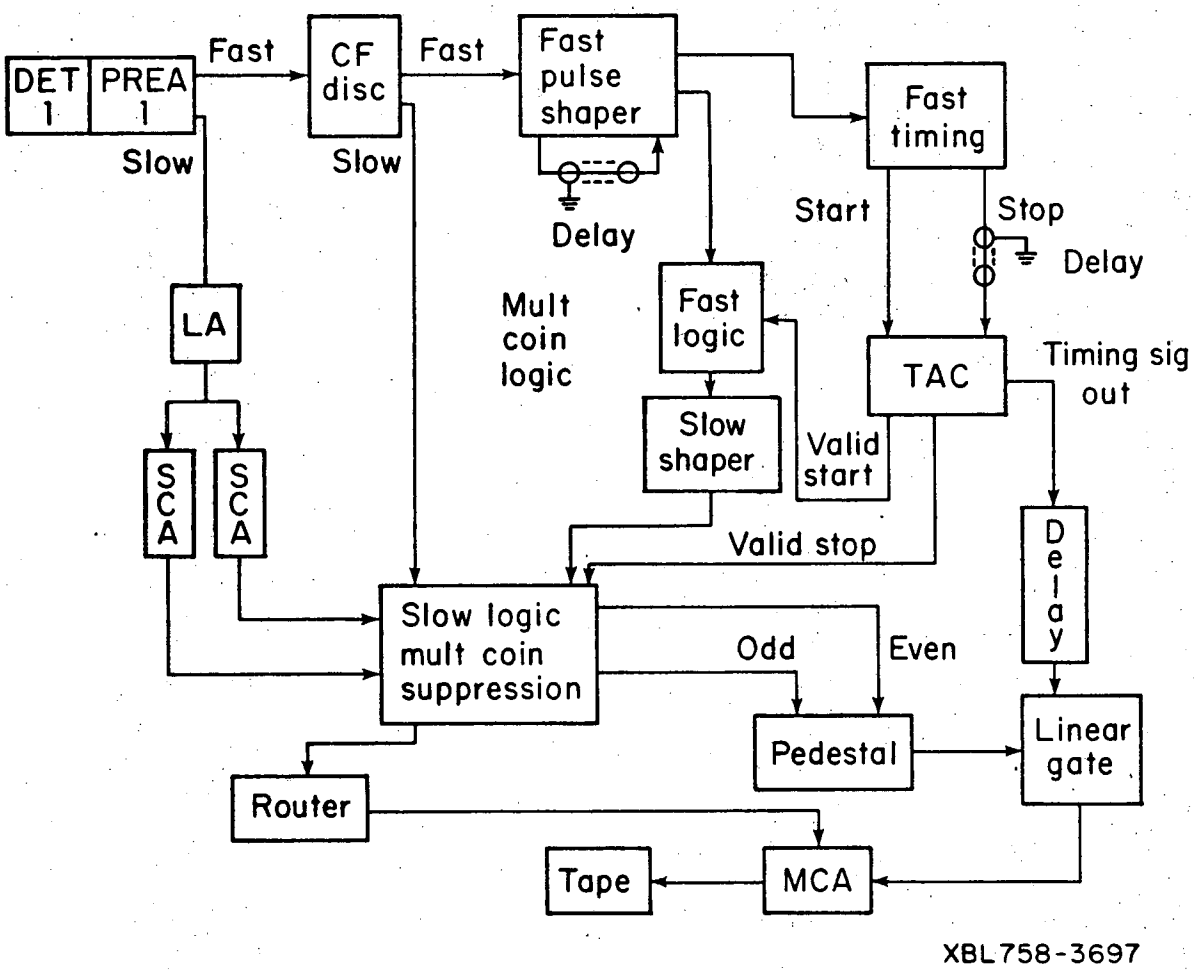
DET 1
PREA 1
Fast
CF disc
Fast
Fast pulse shaper
Fast timing
Slow
Slow
Delay
Start
Stop
Delay
LA
Mult coin logic
Fast logic
TAC
Timing sig out
SCA
SCA
Slow shaper
Valid start
Valid stop
Delay
Slow logic mult coin suppression
Odd
Even
Pedestal
Linear gate
Router
Tape
MCA
XBL758-3697

Fig. III-3.

Packard PHA along with the appropriate routing signals. A Kennedy 1600 tape unit was coupled to the PHA for purposes of data reduction.

The eight-counter system recorded eight 180° and eight 90° spectra and circuit-wise could be split into two (an even and an odd) four-counter systems. The purpose of the pedestal was to add in the even side a region which reflected only chance coincidences. This could not be incorporated into a simple delay box as with the odd side because of the way the TAC was designed. The characteristic time resolution of this system was 1.05-1.15 ns FWHM on ^{22}Na 511-511 cascade with the SCA's set up for the ^{111m}Cd cascade. The Eldorado 610 Digital Delay Generator was used to calibrate the TAC.

C. The High-Pressure Cell, Temperature Regulator, and Miscellaneous Equipment

In order to measure the pressure dependence of the transferred hyperfine field, we built a simple clamping-type pressure cell which is shown schematically in Fig. 4. "Windows" were machined out of the cell in the vicinity of the sample in order to obtain the highest possible coincidence rate. We chose to make the cell body out of A286, a steel which does not fracture at liquid helium temperatures. The clamping nut and backup plugs are also of A286, while the pistons were ground from tungsten carbide. The cell worked reliably to 22 kbar but at pressures around 30 kbar the cell body and inner bore tended to stretch. After something like thirty runs the inner bore had stretched non-uniformly from 187.5 mils to 196 mils. The pressure locked into the cell after tightening the clamping nut was calibrated by measuring the shift in the quadrupole coupling constant for ^{111}In in Cd metal.

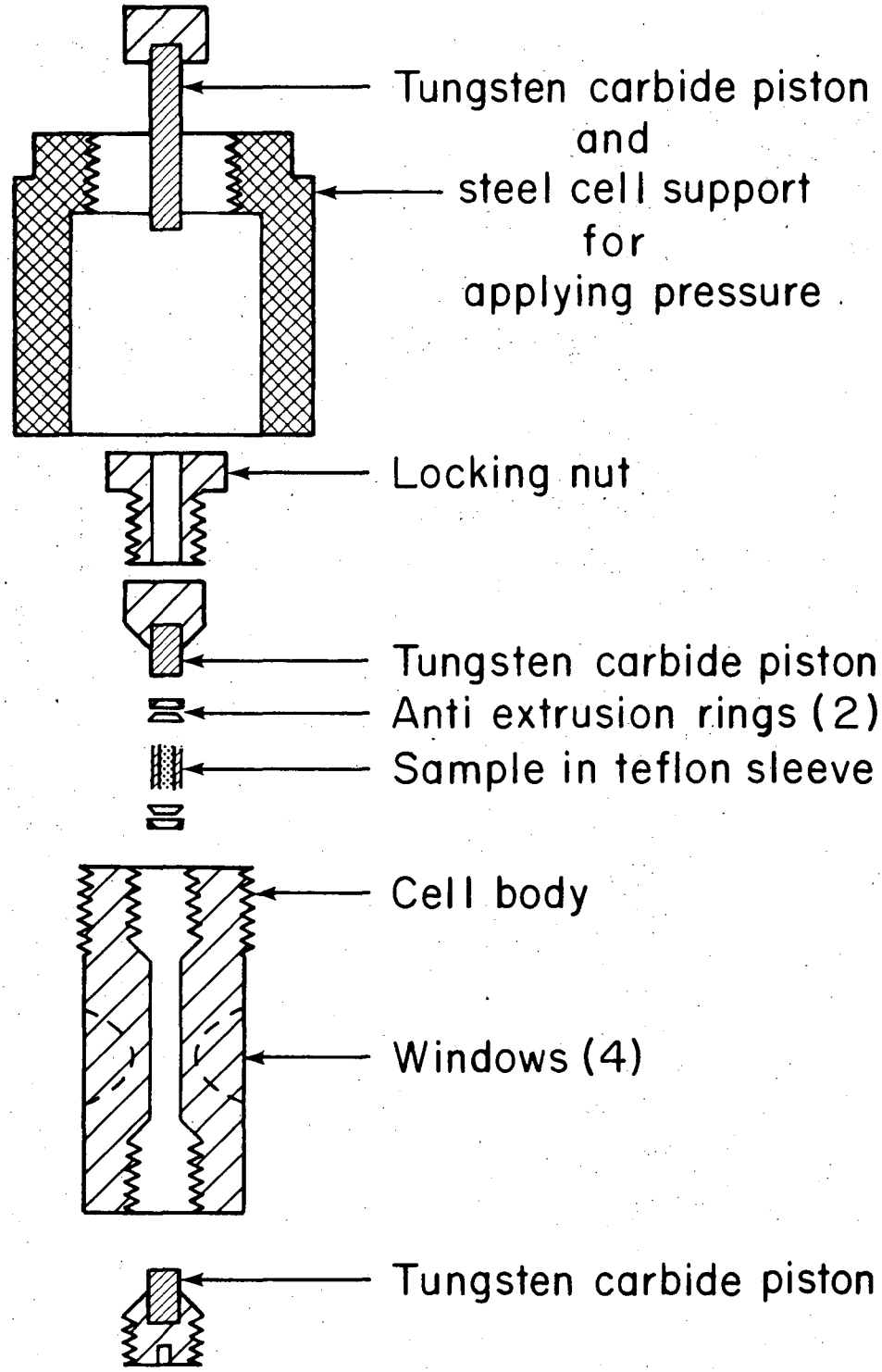

Fig. III-4. XBL 758-3696

For experiments in which the temperature of the sample needed to be regulated, we modified a standard metal dewar with windows for low energy γ-ray counting by necking down the tailstock to ½" id. Into this reduced tailstock we inserted our sample holder and temperature regulator of the type first described by Welber and Tynan.[12] Figure 5 shows our adaptation, which consists of nothing more than a thin-walled stainless steel tube connected to four inches of nylon rod and terminated in a copper bobbin to which the aluminum sample housing was connected. The nylon rod was pressed through a four inch cylinder of styrofoam which fit snugly into the tailstock and prevented liquid helium from passing to the sample holder. The copper bobbin had a heater and Au-Fe thermocouple attached to it for purposes of temperature control and measurement. We calibrated the thermocouple against a germanium thermometer purchased from Cryo Cal, Inc. The calibration of the germanium thermometer was traceable from NBS standards from 1.5 to 100 degrees Kelvin.

Figure 6 shows a simple schematic for the circuit employed in the actual temperature regulation. During a measurement the thermocouple voltage was fixed on a Leeds Northrup K-3 potentiometer and the out of balance signal displayed on a galvanometer. Fluctuations of the out of balance signal were detected by a light sensing diode and fed back into the heater on the copper bobbin. Regulation was stable over several hours to ±0.2° K for temperatures greater than 15° K, but below this temperature the response of the feedback was insufficient to regulate properly.

Two different magnet configurations were used in the work. For the paramagnetic shift experiments a C-frame iron core electromagnet with a

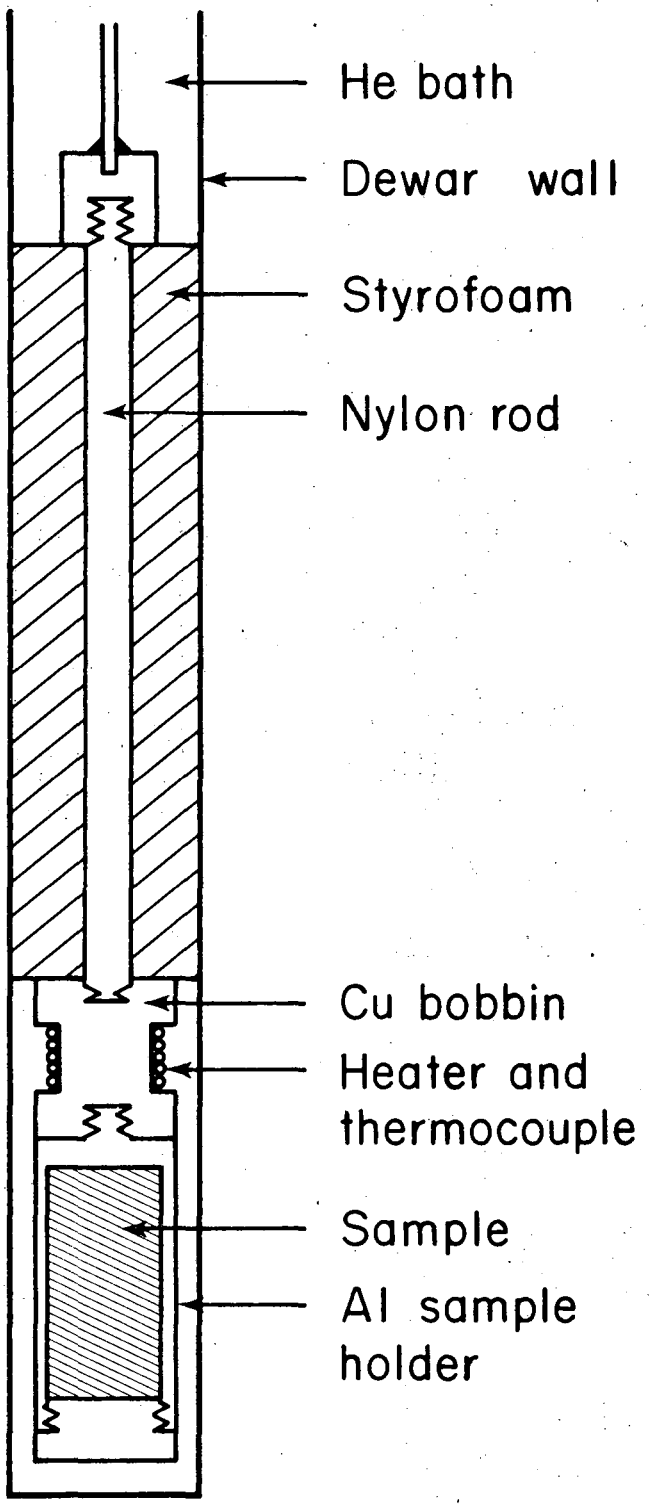

Fig. III-5. XBL758-3695

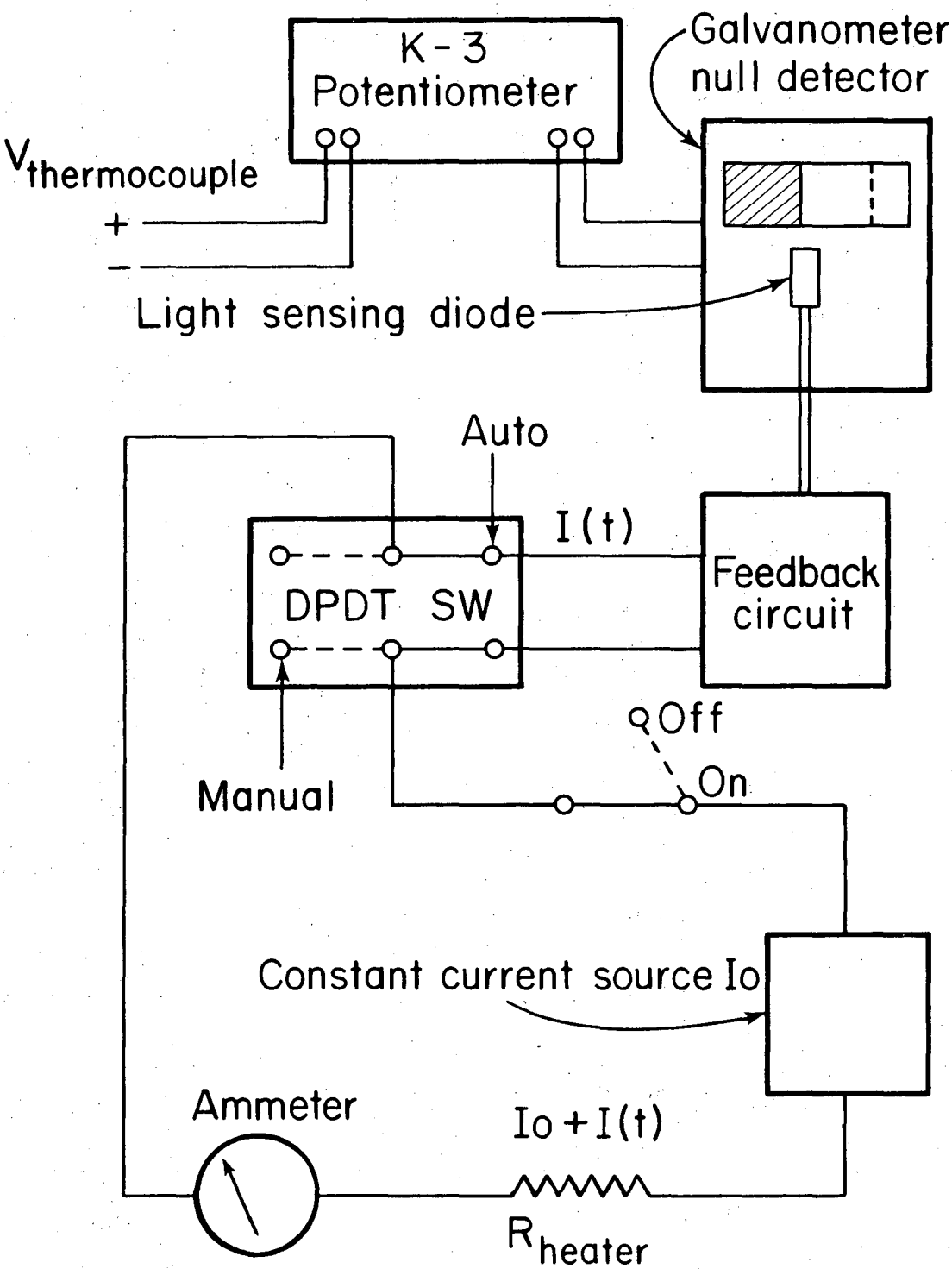

Fig. III-6.

XBL758-3703

maximum field of 38 kOe with a one inch gap sufficed. The magnet was powered by a Spectromagnetic Industries Model TC 200-300 D.C. power supply with a stability of 1% over several days. The spin-flop experiment required counting along the magnetic field axis, and for this purpose we bored out the pole pieces of a small Varian NMR magnet and inserted the counters parallel to the applied field.

The fields of the magnets were measured using a rotating coil gaussmeter which had been calibrated against an NMR probe in a high homogeneity electromagnet. The field errors were principally due to current supply drift and nonreproducible sampling of the volume between the pole pieces.

IV. DATA ANALYSIS

Since the eight-counter circuitry is consistent with a description as two high-speed four counter systems, it shall suffice to describe how the data are analyzed for a set of four counters placed on a square array and labeled cyclically A,B,C,D. If a given detector can function as only a START or a STOP, then there would be two 180° coincidences (AC,BD) and four 90° coincidences (AB,BC,CD,DA). The eight-counter electronics allow a counter to function as both a START and a STOP detector, thereby doubling the number of allowed combinations. In practice all of the 180° spectra are used but only half of the 90° combinations are selected for analysis. The coincidence counting rate between two detectors, e.g. A and C, is related to the polycrystalline correlation function ($k_{max} = 2$) found in Eq. 5 by the following expression

$$N_{AC}(t) = N_0 e^{-t/\tau_N} E_{AC} \{1 + Q_{AC} A_{22} G_{22}(t) P_2(\cos\theta_{AC})\} + C_{AC} \quad (11)$$

N_0 reflects the source strength when the experiment begins, and E_{AC} is an "effective" detector efficiency for the detection of the γ_1-γ_2 pair by NaI(Tl) crystals of fixed thickness. The factor e^{-t/τ_N} describes the fact that even without a perturbation a statistical ensemble of nuclei, each with a mean life τ_N, will decay exponentially. Q_{AC} accounts for the finite solid angle which the detectors subtend, and the constant C_{AC} reflects the background of chance coincidences.

A. Extraction of the Factor $A_{22}G_{22}(t)$

It was realized[13] some time ago that the coincidence counts of the combinations $N_{AC}(180°)$, $N_{BD}(180°)$, $N_{AD}(90°)$, and $N_{BC}(90°)$ could be arranged

in such a way that the source strength N_0, the nuclear lifetime τ_N, and to a good approximation the coincidence efficiencies E_{AC}, etc. could be made to cancel. This is not true if one has only two or three counters, where unequal coincidence efficiencies and solid angle factors necessitate large corrections. This is accomplished by using detectors A and B as STARTS, and C and D as STOPS, and by forming the ratio

$$\frac{2}{3}\left\{\left[\frac{(N_{AC}-C_{AC})\ (N_{BD}-C_{BD})}{(N_{AD}-C_{AD})\ (N_{BC}-C_{BC})}\right]^{\frac{1}{2}}\right\} - 1 \cong \overline{Q}\ A_{22}G_{22}(t)$$

$$\cong \overline{A}_{22}G_{22}(t) \qquad (13)$$

Here $\overline{Q}$ is an average solid angle factor which can be incorporated into the theoretical A_{22} value derived from the spin levels and multiplicities to yield an "effective" amplitude $\overline{A}_{22}$.

B. Least Squares Fitting of $\overline{A}_{22}G_{22}(t)$

Having extracted the factor $\overline{A}_{22}G_{22}(t)$, it is necessary to fit the perturbation in order to obtain the Larmor and quadrupole radial frequencies ω_L and ω_Q. For a pure magnetic interaction the spectra were fit to

$$\overline{A}_{22}G_{22}(t) = \frac{\overline{A}_{22}}{5}\ \{1 + 2\cos\omega_L(t-t_0) + 2\cos 2\omega_L(t-t_0)\} + \text{back.} \qquad (14)$$

and for a pure quadrupole interaction with axial symmetry ($\eta = 0$)

$$A_{22}G_{22}(t) = \frac{\overline{A}_{22}}{5}\ \{1 + \frac{13}{7}\cos\omega_Q(t-t_0) + \frac{10}{7}\cos 2\omega_Q(t-t_0)$$

$$+ \frac{5}{7}\cos 3\omega_Q(t-t_0)\} + \text{Back.} \qquad (15)$$

The fit parameters were $\overline{A}_{22}$, ω_L, ω_Q, t_0, a zero channel for starting the

the digital data, and Back, a background generally due to self-absorption in the samples. Occasionally we experienced a distribution of fields, and this was accounted for by introducing a factor multiplying the $\cos n\omega(t-t_0)$ coefficients by $e^{-|n\omega\sigma(t-t_0)|}$ or $e^{-\frac{1}{2}(\sigma n(t-t_0))^2}$ for Lorentzian or Gaussian distributions. In this case σ, the full width at half maximum, became an additional parameter.

For a quadrupole interaction with a non-zero asymmetry parameter, the ratio of the frequencies in Eq. 15 are no longer 1:2:3. A numerical solution of the secular equation then yielded the eigenvectors for the Hamiltonian. In order to guess a reasonable value for the asymmetry parameter η, we would Fourier transform the data in order to extract the ratios of the frequencies $\omega_1:\omega_2:\omega_3$. These ratios could then be compared with the derived[14] ratios for various values of η for a spin 5/2. It was generally necessary to have an initial guess for the parameter values which was fairly close to the true values in order for the fitting program to converge. This was especially true when performing five and six parameter fits.

For the general case of combined interactions, the Fourier transform of the autocorrelation function of the digital data was taken and compared with a set of computer generated theoretical curves for various values of the magnetic field and electric field gradient parameters. It was necessary to run the spectrum above the magnetic transition in order to obtain a value for ω_Q and η which would be close to the ones obtained in the liquid helium spectra. It was also necessary to guess the angle θ between the principal axis of the electric field gradient and the internal magnetic field from symmetry considerations. With those constraints one could

run theoretical Fourier transform spectra as a function of internal magnetic field only and compare them to the experimental transforms. This matchup would then constitute a set of initial guesses for the parameters in the least squares fitting routine.

ACKNOWLEDGEMENTS

At this point is is natural to stop and reflect on the years spent in any thesis effort. My parting impressions are concerned less with the projects undertaken than with the many people who helped to share and shape the experiences of the last several years. It is with particular gratitude that I wish to thank David A. Shirley and Herbert Rinneberg for their guidance, patience and encouragement in directing my research. Of no less importance are those close friends and acquaintances whose contributions cannot be weighed in terms of ideas shared or technical support rendered. I take a special pleasure in thanking Baylor and Linda Triplett, Larry Bernstein, Wini Heppler, Gerda Bolz, Betty James and Gus Apai for helping to make the years pass in a pleasant and friendly fashion. I would also like to single out those technical support groups whose energy and competence place them above the already excellent levels available at LBL. Accolades are due the entire staff of the Chemistry Department Machine Shop, the Health Chemistry monitors who regularly participated in my target preparations, and Ruth Mary Larimer and Harry Harrington of the 88 inch LBL cyclotron.

REFERENCES

1. Linus Pauling, J. Am. Chem. Soc. 53, 1367 (1931); Phys. Rev. 37, 1185 (1931); J. Am. Chem. Soc. 54, 988 (1932).

2. J. H. Van Vleck, Phys. Rev. 41, 208 (1932).

3. H. A. Kramers Physica 1, 182 (1934).

4. P. W. Anderson, Solid State Phys. 14, 99 (1963); Informal Proc. Buhl Intern. Conf. Mater. Pittsburgh, p. 17 (1963).

5. H. Frauenfelder and R. M. Steffen, Angular Correlations in Alpha-, Beta-, and Gamma-Ray Spectroscopy, K. Siegbahn, editor (North Holland Pub. Co., Amsterdam, 1965), p. 997 ff.

6. E. Karlsson, E. Matthias, and K. Siegbahn, editors, Perturbed Angular Correlations (North Holland Pub. Co., Amsterdam, 1964).

7. D. M. Brink and G. R. Satchler, Angular Momentum (Clarendon Press, Oxford, 1968).

8. S. G. Cohen, Chap. 12, Hyperfine Interactions, A. J. Freeman and R. B. Frankel, editors, (Academic Press, New York, London, 1967).

9. A. J. Ferguson, Angular Correlation Methods in Gamma-Ray Spectroscopy (North Holland Pub. Co., Amsterdam, 1965).

10. M. R. Maier and P. Sperr, Nucl. Instr. Methods 87, 13 (1970).

11. T. R. Gerholm, Z. H. Cho, L. Eriksson, L. Gidefeldt, and B. G. Pettersson, Nucl. Instr. Methods 100, 33 (1972).

12. B. Welber and E. E. Tynan, Rev. Sci. Instrum. 38(1), 137 (1967).

13. B. Erik Karlsson, Arkiv. Fysik 22, 1 (1962).

14. E. Gerdau, J. Wolf, H. Winkler, and J. Braunsfurth, Proc. Roy. Soc. A. 311, 197 (1969).

FIGURE CAPTIONS

Fig. 1. Two photon decay cascades for ^{111m}Cd and ^{111}In used in this work.

Fig. 2. Electronic schematic of the four-counter system showing the components and their sequencing.

Fig. 3. Block diagram for a single NaI(Tl) counter in the eight-counter system showing the electronic sequencing of the fast and slow signals.

Fig. 4. High pressure clamping type pressure cell. The body is constructed of A286 steel and four "windows" have been machined in the vicinity of the sample to reduce gamma-ray attenuation.

Fig. 5. The temperature regulator employed in the sublattice magnetization experiments shown enclosed in the tailstock of a liquid helium dewar.

Fig. 6. Block diagram of the temperature regulator electronics. The light sensing diode was linked to a feedback circuit which pulsed the sample heater and regulated the temperature over several hours to $\pm 0.2^{\circ}K$.

V. SYSTEMATICS OF HYPERFINE FIELDS OBSERVED BY PAC IN Cd-DOPED TRANSITION METAL ANTIFERROMAGNETS*

A. INTRODUCTION

The properties of the simple 3d transition metal salts with d^5 through d^{10} configurations are generally consistent with localized electron behavior,[1] for which LCAO-MO calculations can describe the nature of the chemical bonding with reasonable success. Within the framework of the MO model, we have examined the systematic variation of the hyperfine fields transferred through the ligands into a diamagnetic dopant (^{111m}Cd) for the transition metal using γ-ray perturbed angular correlation (PAC). The variations of the MO spin density parameters with changes in both the ligand and the transition metal are correlated with the transferred hyperfine fields.

The PAC data are complementary to those previously derived from NMR, ESR, ENDOR, neutron diffraction, and Mössbauer techniques, but there are differences among the methods which deserve some comment. Especially relevant to PAC is a symmetry argument[2] based on the assumption that the hyperfine field at the Cd impurity is primarily derived from overlap and covalency effects of the Cd ns shells. The symmetry of the s shells leads to PAC being σ,s bond specific. For d^5 ions the importance of this difference is highlighted by the measurements of NMR, ENDOR, and ESR, which measure $f_\sigma - f_\pi$, and for neutron diffraction which measures $2f_\pi + f_\sigma + f_s$. This has hampered the understanding of the Mn compounds, because f_σ and f_π are generally of the same order of magnitude. Mössbauer spectroscopy and

---

*This section of work was done in conjunction with H.H. Rinneberg and D. A. Shirley

PAC are potentially competitive, but there has been little overlap due to the limitations on available Mössbauer nuclei which can be used to replace the transition metal substitutionally.

There is an additional problem concerning the comparison of data collected in magnetically dilute (ENDOR, ESR) and magnetically concentrated (NMR, neutron diffraction, PAC, Mössbauer) systems. Our data are consistent with the view that it is valid to compare derived spin density parameters between dilute and concentrated systems within the experimental errors inherent in the data analysis.

Experimental details are given in Section B, while Section C outlines the MO model and inherent limitations in its application to the properties of these salts. Section D contains our results and their interpretation relative to the MO model.

B. EXPERIMENTAl

1. Detector System

Data for this study were accumulated on both four and eight counter γ-γ coincidence spectrometers which have previously been described.[3,4] Both systems employ the familiar fast-slow logic, and only 180° and 90° correlations were observed and combined to yield the perturbation factor independent of counter efficiencies and the lifetime of the intermediate nuclear state.[5]

Standard 1×1½" NaI(Tl) crystals were used as photon detectors for the ^{111m}Cd cascade. The time-to-amplitude converters for the two spectrometers were calibrated with cables and an Eldorado 610 digital delay generator. With the single channel analyzer windows set on the ^{111m}Cd energies (150,247 keV), the time resolution using ^{22}Na 511-511 radiation

was 1.8 and 1.1 ns FWHM for the four and eight counter spectrometers respectively.

2. Sample Preparation

The preparation of some of the compounds ($KNiF_3$, $KCoF_3$, $RbMnF_3$;[2] MnO, CoO, NiO)[4] had been described previously. In general the ^{111m}Cd was obtained by neutron irradiation of ^{110}CdO, converted to the appropriate dihalide by dissolving in acid and evaporating to dryness, and subsequently thermally diffused into the fluorides and chlorides listed in Tables 1A and 1B. Since the A_2MX_4 compounds melt incongruently, it was necessary to sinter the activity in at temperatures well below the peritectic. The remaining chlorides and fluorides melt congruently. Single-phase samples were obtained by diffusing the activity into the lattice at temperatures close to the melting points. The hygroscopic nature of many of the reactants required us to perform the preparative operations under dry nitrogen conditions.

The double fluorides and chlorides AMX_3 and A_2MX_4 were prepared by the corresponding solid-state reactions:

$$AX + MX_2 \xrightarrow[\Delta]{\text{melted}} AMX_3, \text{ and } 2AX + MX_2 \xrightarrow[\Delta]{\text{sintered}} A_2MX_4. \qquad (1)$$

High purity, anhydrous KF, RbF, RbCl, CoF_2, and MnF_2 were commercially available. TlF was prepared by dissolving 99.999% Tl metal in aqueous HF. The product was dried by melting in a platinum cruicible under vacuum. Anhydrous CuF_2 and NiF_2 were obtained by passing F_2 over the respective anhydrous dichlorides at 400 °C. Anhydrous FeF_2 was prepared from $FeCl_2$ in a stream of dry HF gas at 650 °C. The transition metal dichlorides had previously been prepared by the dehydration of $MnCl_2 \cdot 4H_2O$, $FeCl_2 \cdot 4H_2O$

by a stream of HCl gas at 200-300 °C.

α-MnS doped with activity was obtained by coprecipitation under an oxygen-free atmosphere following the procedure given by Brauer.[6] The precipitate was dried and then heated to 1000 °C in a platinum tube under H_2S.

3. Data Analysis

For a polycrystalline sample with unique but randomly-oriented axes, the perturbed angular correlation for a γ-γ cascade is given by[7]

$$W(\theta,t) = \sum_{k \text{ even}} A_{kk} G_{kk}(t) P_k(\cos\theta). \qquad (2)$$

For the ^{111m}Cd cascade it is sufficient to truncate the series at k = 2 yielding for a normalized correlation

$$W(\theta,t) = 1 + A_{22} G_{22}(t) P_2(\cos\theta). \qquad (3)$$

Here A_{22} is the anisotropy of the 150-247 keV cascade, $P_2(\cos\theta)$ is the second Legendre polynomial associated with the angle θ between the direction of the two gamma rays, and $G_{22}(t)$ is the polycrystalline perturbation factor. This function is obtained from the magnetic and electric hyperfine interactions of the Cd nucleus in the intermediate 247-keV state ($I = 5/2$, τ_N = 121 nsec). For a pure magnetic dipole interaction one obtains an analytical function for the perturbation factor[7]

$$G_{22}(t) = \frac{1}{5}\{1 + 2\cos(\omega_L t) + 2\cos(2\omega_L t)\} \qquad (4)$$

with $\omega_L \equiv \frac{g_N \mu_n H_{int}}{\hbar}$. i.e., the Larmor precession frequency of the nuclear moment due to the internal magnetic field H_{int}.

In the more general case of a combined magnetic dipole and electric quadrupole interaction, the perturbation factor $G_{22}(t)$ can still be

calculated as a sum of cosine terms[7] after obtaining the eigenvalues of the Hamiltonian

$$H = - g \mu_n \vec{H}_{int} \cdot \vec{I} + \frac{e^2 q_{zz} Q}{4I(2I-1)} \{3I_z^2 - I(I+1) + \eta(I_x^2 - I_y^2)\} \qquad (5)$$

The components of $\vec{I}$ refer to the principal axes of the field gradient tensor (eq_{xx}, eq_{yy}, eq_{zz}) and η is the asymmetry parameter defined by $\eta = \frac{q_{xx} - q_{yy}}{q_{zz}}$.

In general only for pure magnetic dipole and pure quadrupole interaction with axial symmetry ($\eta = 0$) will the frequencies contained in $G_{22}(t)$ be integral multiples of each other and a periodic oscillation of the intensity of the second γ-radiation be observed. For an asymmetric electric field gradient or a combined magnetic dipole-electric quadrupole interaction, the transition frequencies are no longer overtones of a single frequency due to the shifts of the energy levels of the Hamiltonian, and $G_{22}(t)$ becomes an aperiodic function of time. The spectrum of $KCuF_3$ in the paramagnetic state displays (Fig. 1) a non-axial electric field gradient, while K_2NiF_4 (Fig. 2) at 4.2°K shows a combined interaction in the antiferromagnetic state, for which the hyperfine field of the impurity is parallel to the unique axis of the field gradient. In order to analyze combined interactions, it is of considerable advantage to calculate[8] the power spectral density $P(\omega)$ of the perturbation factor rather than $G_{22}(t)$ itself. This is illustrated in Fig. 3 for K_2NiF_4 where the solid line represents a least-squares fit of the power spectral density to that obtained from the experimental data (dotted line).

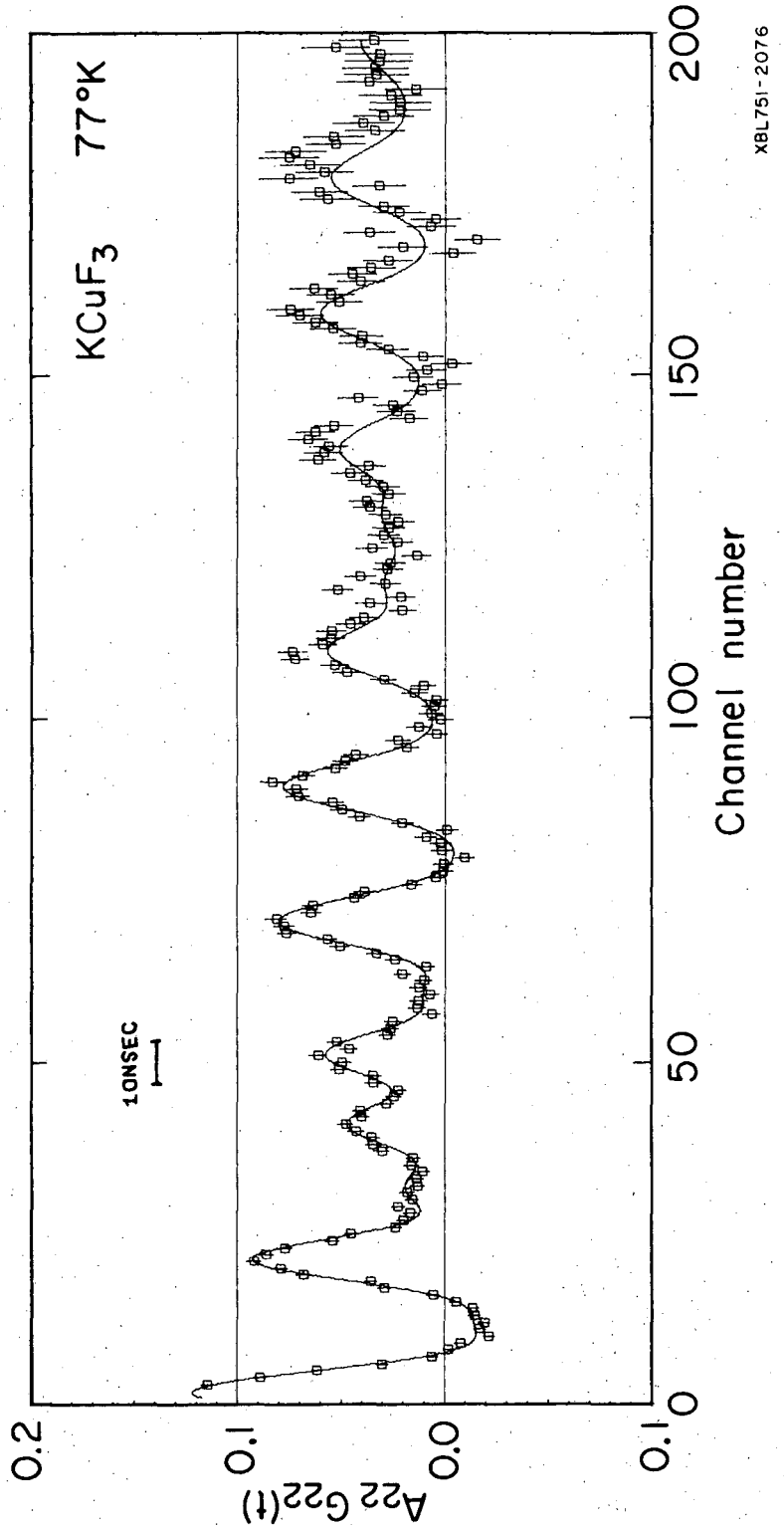

Fig. V-1.

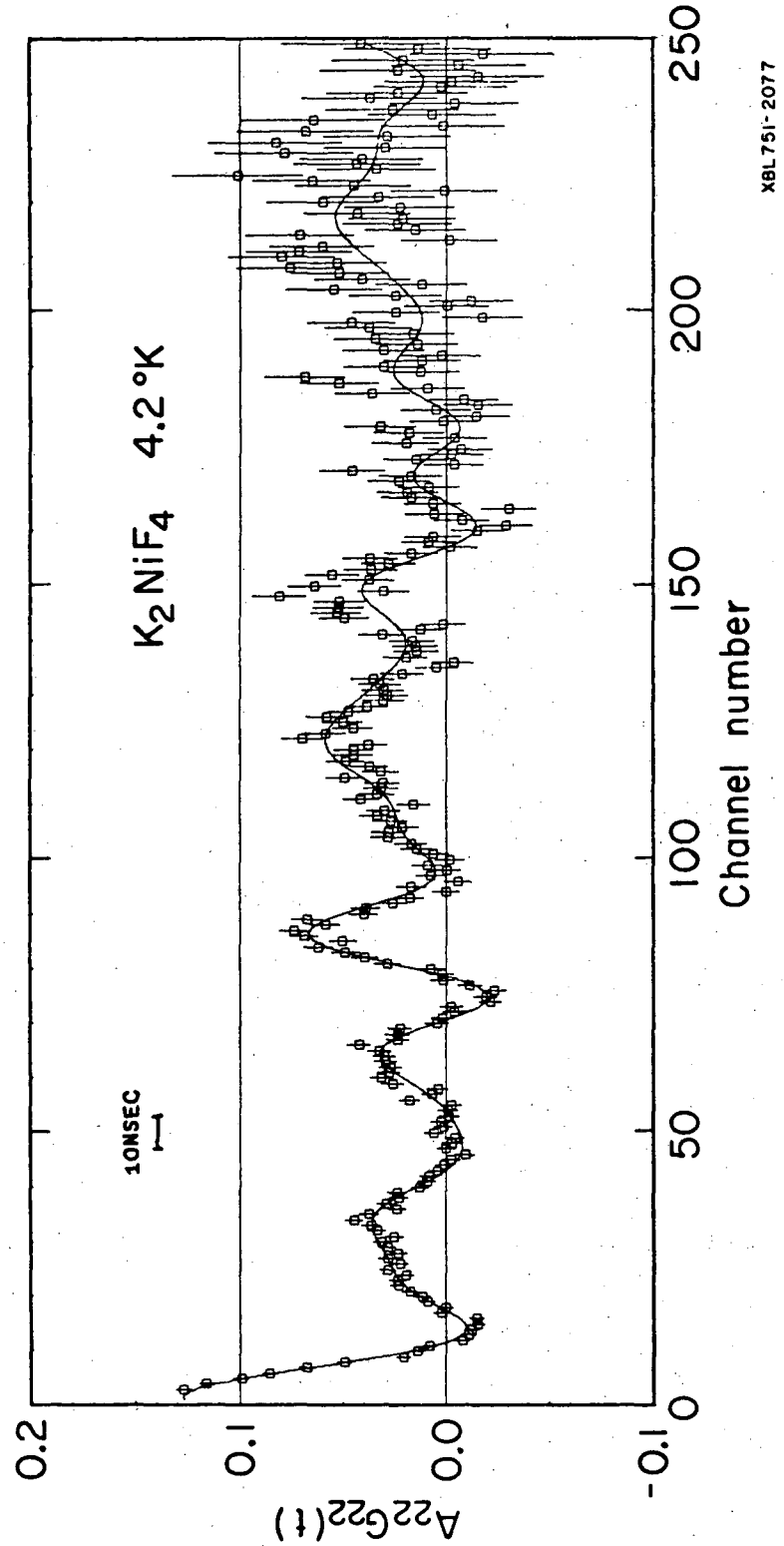
K_2NiF_4 4.2°K
10NSEC
$A_{22}G_{22}(t)$
0.2
0.1
0.0
-0.1
0
50
100
150
200
250
Channel number
XBL751-2077

Fig. V-2.

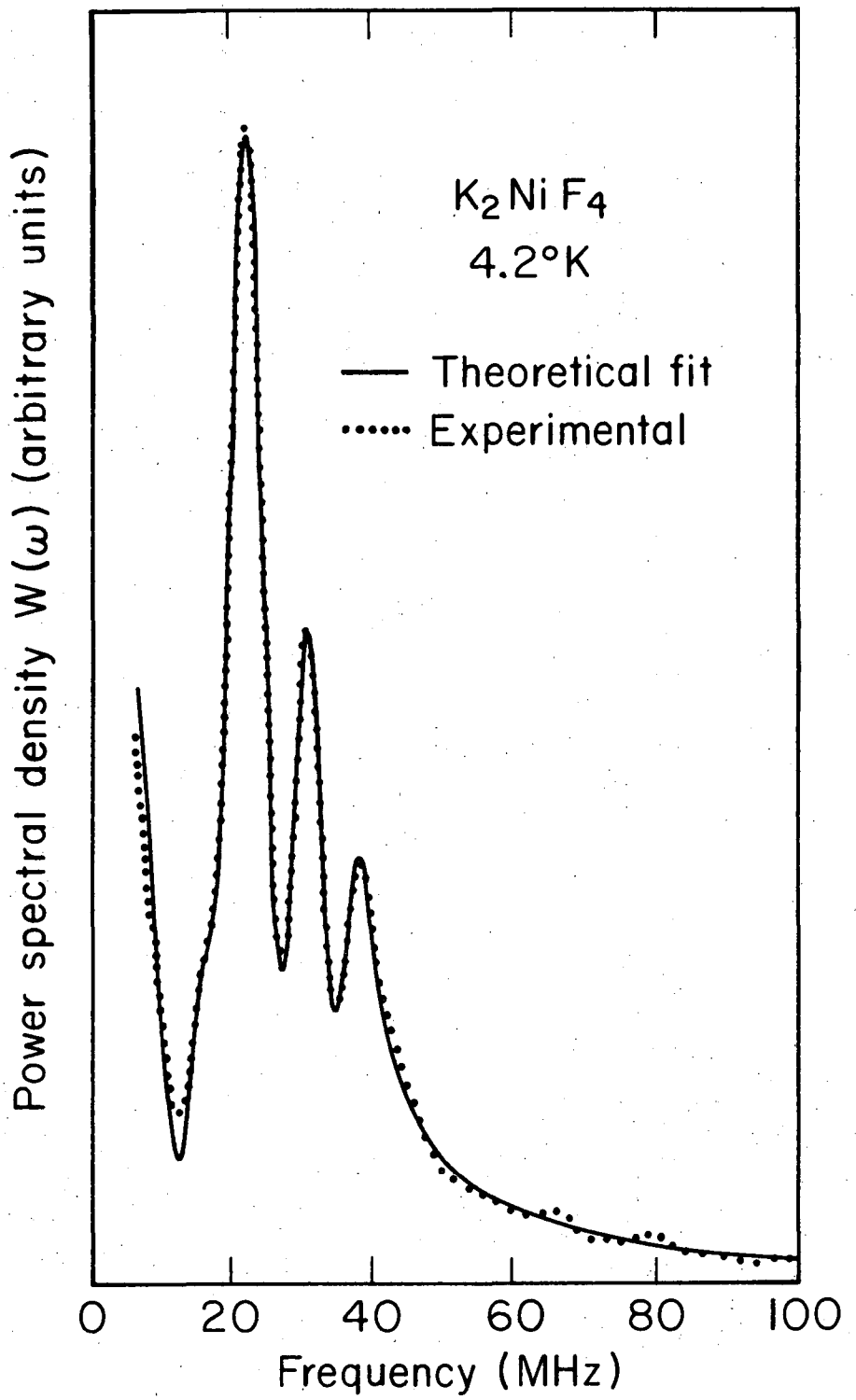

Fig. V-3. XBL758-3702

Tables IA,B contain the results of our measurements in insulating antiferromagnets.

C. LCAO-MO MODEL

Considerable theoretical effort[9,10,11,12,13] has gone into understanding the electronic energy level diagram of the octahedrally coordinated 3d transition metal cluster $(ML_6)^{-q}$, primarily with L = F^- or O^{2-}. We will assume the basic correctness of the energy level diagram of Fig. 4 and focus on the properties of the sigma bonds possible between the metal ion and the ligands.

The filled bonding orbitals are primarily of ligand character,

$$\psi_\sigma^B = N_\sigma^B(\chi_{p\sigma} + \gamma_\sigma d_\sigma + \gamma_s \chi_s), \tag{6}$$

where $\chi_{p\sigma}$, χ_s are symmetry-allowed linear combinations of ligand s, pσ orbitals, and γ_σ, γ_s are covalency mixing parameters which describe the admixing of metal d_σ orbitals into the ligand p_σ, s orbitals. The ligand orbitals are generally restricted to $2p_\sigma$ and 2s for F^- and O^{2-}, and $3p_\sigma$ and 3s for Cl^- and S^{2-}.

The partially-filled antibonding orbitals are mainly metal-like, and contribute to the magnetic properties.

$$\psi_\sigma^A = N_\sigma^A \{d_\sigma - (\lambda_\sigma \chi_{p\sigma} + \lambda_s \chi_s)\} . \tag{7}$$

Normalization and orthogonality of bonding and antibonding orbitals are used to derive relations connecting the parameters. To first order one obtains

$$\lambda_\sigma = \gamma_\sigma + S_\sigma \quad \text{and} \quad \lambda_s = \gamma_s + S_s . \tag{8}$$

Tables I. A,B. Magnetic and quadrupole interactions of ^{111m}Cd in insulating host antiferromagnets

I.A. Host materials with 3 dimensional magnetic structure

Host	T_N (K)	H_{exp} (KΘe±1.5)	H_{hf} (KΘe±2.5)	ν_Q (MHz±0.2)	η	Crystal structure	Magnetic structure	Remarks
$KMnF_3$	95	102.6		0	0		Complex	Spin canting
$RbMnF_3$	83	113.8	117.4	0	0		G	No distortions
$TlMnF_3$	76	118.7	122.5	0	0		G	
$KFeF_3$	112.5	100.1	104.2	0	0	Perovskite	Complex	Spin canting
$KCoF_3$	114	74.1	78.2	0	0	$KNiF_3$ type	G	Small lattice distortions
$RbCoF_3$	~101	67.8	71.5	0	0			
$TlCoF_3$	94	67.9	71.6	0	0			
$KNiF_3$	253	104.8	113.7	0	0		G	No distortion
$KCuF_3$	38,20	< 4		19.3	0.74	$KCuF_3$	A	2 Modifications
MnO	~118	202	208	0	0	NaCl	MnO	$\vec{S} \parallel \langle 111 \rangle$
CoO	~293	177	187	0	0		Complex	
NiO	~520	196	212	0	0		MnO	$\vec{S} \parallel \langle 111 \rangle$
$FeCl_2$	23.5	4.8		5.8	0	$CdCl_2$	$\vec{S} \parallel C$	
$CoCl_2$	25	~ 0		5.8	0		$\vec{S} \perp C$	
α-MnS	156	244.4	258	0	0	NaCl	MnO	

Table I.B. Host materials with 2 dimensional magnetic structure

Host	T_N °K	H_{exp} (KOe ±1.5)	H_{hf} (KOe ±2.5)	ν_Q (MHz ±0.2)	η	Crystal structure	Magnetic structure	Remarks
K_2MnF_4	~45	71.6	79.4	3.4	0	↑	↑	Heisenberg antiferromagnets
Rb_2MnF_4	38.5	67.9	75.4	4.7	0	↑	↑	Heisenberg antiferromagnets
K_2CoF_4	107	51.5	52.7	5.5	0	↑	↑	Ising systems– no zero pt spin deviation dipole correction only
Rb_2CoF_4	101	48.9	50.0	8.2	0	K_2NiF_4	$\vec{S} \parallel C$	Ising systems– no zero pt spin deviation dipole correction only
K_2NiF_4	~97	54.9	69.3	3.7	0	↓	↓	Heisenberg
Rb_2NiF_4	95	51.3	64.7	7.4	0	↓	↓	Heisenberg
Rb_2MnCl_4	57	97.4	106.7	8.1	0	↓	↓	Antiferromagnets

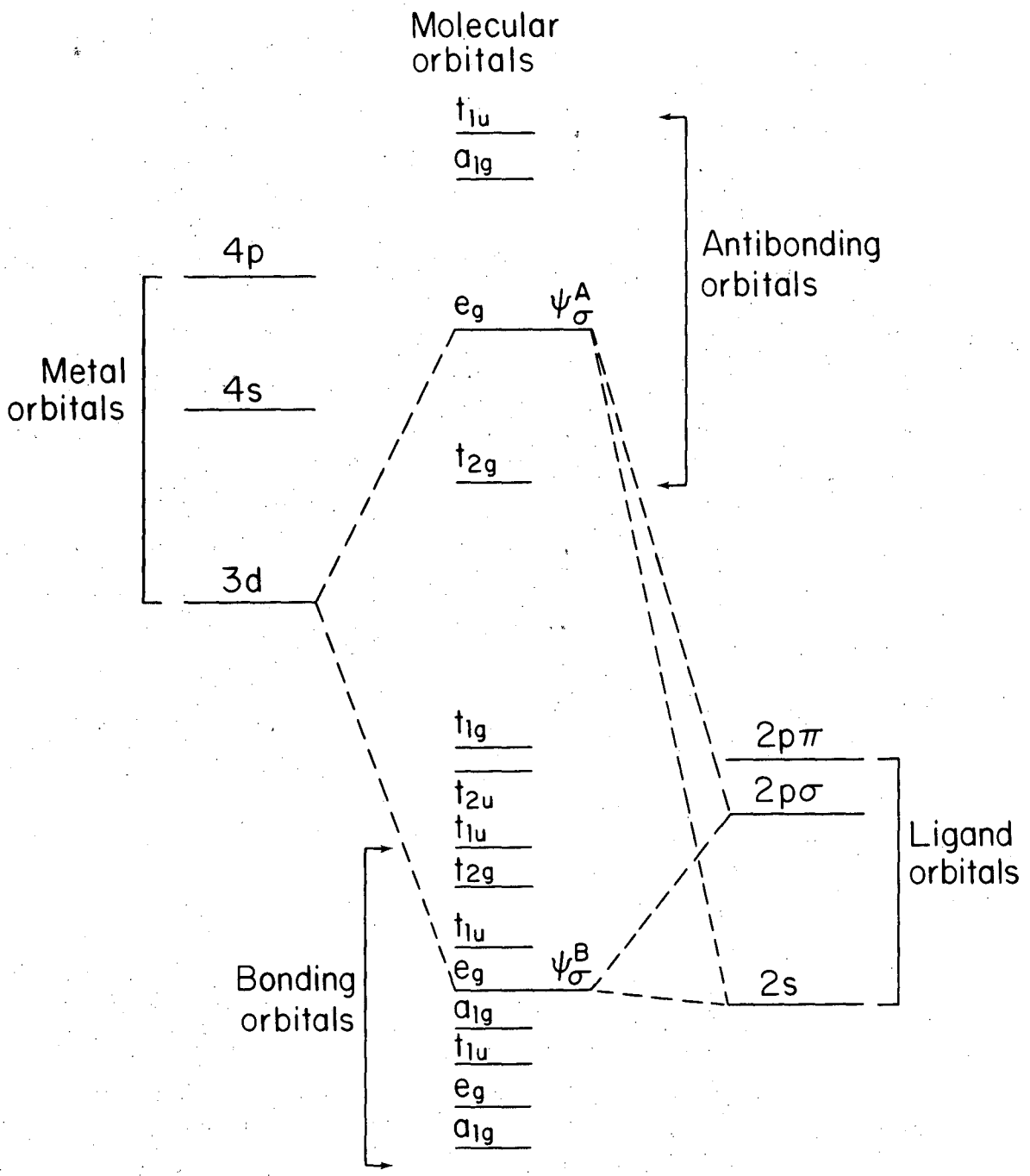

Fig. V-4.

The overlap integrals S_σ and S_s come from the normalization procedure. They are defined by $S_\sigma = \langle d_\sigma | \chi_{p\sigma} \rangle$ and $S_s = \langle d_s \mid \chi_s \rangle$.

The unpaired σ spin density at the liegand has been the object of numerous experimental endeavors because its precise determination is fundamental to theoretical efforts to understand the bonding in these compounds. Using the framework of the LCAO-MO model, Sawatzky and coworkers[14,15,16] have pointed out the necessity of considering the entire extended octahedral complex (see Fig. 5) in order to obtain the correct normalization constants for the cluster. This is in contrast to treating the problem as six separate bonds and multiplying the final calculated hyperfine fields by six.

Following Sawatzky's extended cluster calculation and adapting his results to 180° metal-ligand-Cd exchange paths, we obtain for the supertransferred hyperfine field at the Cd nucleus

$$H_{hf} = -\frac{8\pi}{3}\mu_\beta \cdot 6 \frac{\langle S_z \rangle}{S} N_+^2 N_-^2 \lambda_\sigma^2 \{-\sum_{n=1}^{4} \langle ns | p\sigma \rangle \phi_{ns}(0) + a_{5s}\phi_{5s}^{(0)}\}^2 \quad (9)$$

where $\lambda_\sigma \equiv \gamma_\sigma + \langle p\sigma \mid d_{z^2} \rangle$ and

$$(N_+)^{-2} \tilde{=} (N_-)^{-2} + \lambda_\sigma^2$$

$$(N_-)^{-2} = 1 - 6 \sum_{n=1}^{4} \langle ns | p\sigma \rangle^2 + 6a_{5s}^2 + 12\, a_{5s} \langle 5s \mid p\sigma \rangle - \langle p\sigma | d_{z^2} \rangle^2 \quad (10)$$

In this formulation we have omitted the contribution of the ligand s orbitals to the σ bonding and have neglected ligand three-center overlaps. The parameter a_{5s} allows for a charge transfer into the unoccupied Cd^{2+} 5s orbital yielding a total 5s occupation number of

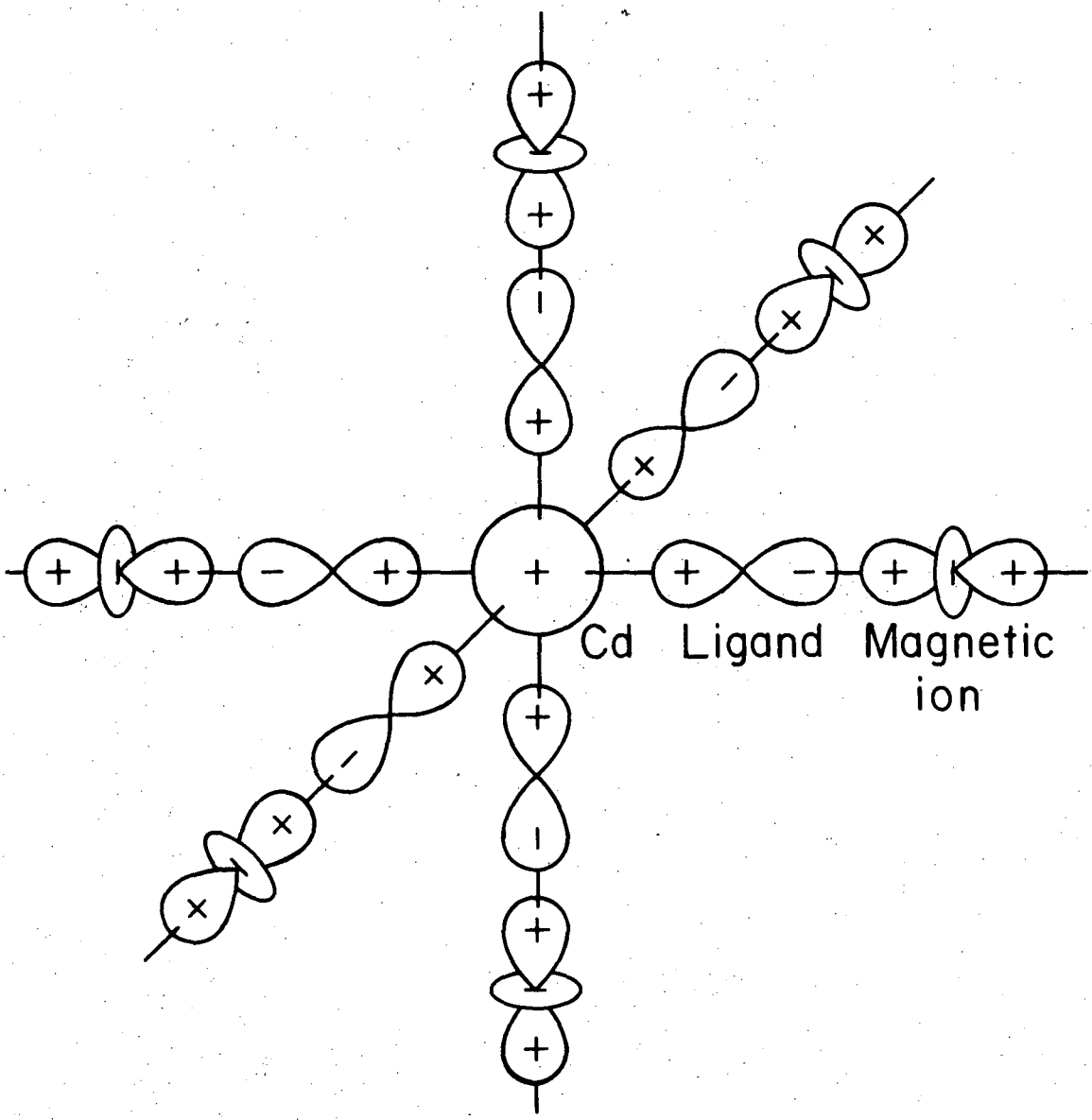

Fig. V-5.

XBL 758-3694

$6(N_+^2 + N_-^2)a_{5s}^2$. Direct metal-Cd overlaps have also been set to zero. The unpaired sigma spin density at the ligand is given by $f_\sigma = \lambda_\sigma^2 N_+^2 N_-^2$.* Tables 2 and 3 tabulate our calculated two-center Cd ns - ligand p overlaps and the metal-ligand overlaps.

Certain limitations involved in calculating the hyperfine fields via Eq. 9 deserve comment. Primary among these is the propriety of using free ion wavefunctions in a solid for the ligands and 3d metals. The overlap integrals with a fixed bond distance are very sensitive to the choice of wavefunctions, and Table 4 shows a comparison using three different choices for the O^{2-} wavefunction. In this work we have chosen to use the numerical HF Cd functions of Mann,[17] and Clementi's[18] functions for F^-, Cl^-, and the transition metals Mn^{2+}, Co^{2+}, and Ni^{2+}. For O^{2-} functions we use the results of Yamashita and Asano[19] as tabulated in Table X of their publication.

One also needs the value of the Cd wavefunctions at the origin, $\phi_{ns}(0)$. These can be obtained empirically starting from Mann's[17] non-relativistic neutral Cd functions. Using the tabulated value for $\phi_{5s}(0)$, we have estimated the hyperfine field for a single 5s electron to be $-\frac{8\pi}{3}\mu_\beta |\phi_{5s}(0)|^2 = 3.59$ MOe, compared to 6.8 MOe obtained from the ESR[20] of $Cd^+(4d^{10}5s^1)$ in KCl. One expects the non-relativistic wavefunctions to be in error for high Z atoms so the lack of agreement is not surprising. In order to correct for this, the density of all the $\phi_{ns}(0)$ functions was adjusted by the factor 6.8/3.59 in lieu of data for the individual ns shells.

---

*In a cluster calculation $N^4 \sim 0.3$, while in the independent-bond model N is usually taken to be 1.

Table II. Cadmium-Ligand Overlap Integrals

A. Fluorides $KNiF_3$ Ni-F = 2.01 Å

$KCdF_3$ Cd-F = 2.15 Å

$\langle Cd\ ns | F^- 2p\sigma \rangle$

	Cd-F = 2.02 Å	Cd-F = 2.15 Å
$\langle 1s \mid 2p\sigma \rangle$	0.000752	0.000594
$\langle 2s \mid 2p\sigma \rangle$	0.004965	0.003933
$\langle 3s \mid 2p\sigma \rangle$	0.019474	0.015433
$\langle 4s \mid 2p\sigma \rangle$	0.080115	0.063960
$\langle 5s \mid 2p\sigma \rangle$	0.191036	0.25478

B. Oxides NiO Ni-O = 2.09 Å

CdO Cd-O = 2.34 Å

$\langle Cd\ ns | O^{2-} 2p\sigma \rangle$

	Cd-O = 2.09 Å	Cd-O = 2.34 Å
$\langle 1s \mid 2p\sigma \rangle$	0.000796	0.000463
$\langle 2s \mid 2p\sigma \rangle$	0.005262	0.003183
$\langle 3s \mid 2p\sigma \rangle$	0.020661	0.012575
$\langle 4s \mid 2p\sigma \rangle$	0.084613	0.053453
$\langle 5s \mid 2p\sigma \rangle$	0.209600	0.194483

(continued)

Table II. (continued)

C. Chlorides	Rb_2CdCl_4	Cd-Cl = 2.60 Å
	$\langle$Cd ns|Cl$^-$ 3pσ$\rangle$	
	Cd-Cl = 2.60 Å	
$\langle$1s 3pσ$\rangle$	0.000667	
$\langle$2s 3pσ$\rangle$	0.004420	
$\langle$3s 3pσ$\rangle$	0.017280	
$\langle$4s 3pσ$\rangle$	0.070140	
$\langle$5s 3pσ$\rangle$	0.173920	

Table III. Metal-Ligand Overlaps

$\langle Mn^{2+}\ d_{z^2} \mid F^- 2p\sigma \rangle = -0.0688$	($KMnF_3$)
$\langle Mn^{2+}\ d_{z^2} \mid O^{2-} 2p\sigma \rangle = -0.0712$	(MnO)
$\langle Mn^{2+}\ d_{z^2} \mid Cl^- 3p\sigma \rangle = -0.06117$	(Rb_2MCl_4)
$\langle Co^{2+}\ d_{z^2} \mid F^- 2p\sigma \rangle = -0.0638$	($KCoF_3$)
$\langle Co^{2+}\ d_{z^2} \mid O^{2-} 2p\sigma \rangle = -0.0657$	(CoO)
$\langle Ni^{2+}\ d_{z^2} \mid F^- 2p\sigma \rangle = -0.0602$	($KNiF_3$)
$\langle Ni^{2+}\ d_{z^2} \mid O^{2-} 2p\sigma \rangle = -0.0621$	(NiO)

Table IV.

$\langle Cd\ 4s | O^{2-}\ 2p\sigma \rangle$

Cd-O = 2.34 Å

O^{2-} wave functions

Yamashita[a]	Watson[b]	Huzinaga[c]
0.05345	0.06943	0.07798

[a] Ref. 19

[b] Ref. 39

[c] Ref. 40

A limitation inherent in working with impurity doped samples is that the exact Cd-ligand bond distance is not known in the compounds. We have considered the two extremes possible, i.e. Cd-ligand distances representative of Cd compounds which are crystallographically isomorphous with the magnetic host materials, and the case where the Cd-ligand distance is taken equal to the metal-ligand distance of the magnetic host. A calculation of the hyperfine field for $KNiF_3$ for which f_σ is known from NMR[21] is shown in Table V. Overlaps were computed for the bond distances characteristic of Cd-F in $KCdF_3$ and for the Cd-F distance equal to the Ni-F separation. An intermediate Cd-ligand distance is probably the most realistic assumption. Even with the "short" bond distance the field calculated using all the Cd ns shells is lower than the experimental value by 20%, and for the "long" bond length the calculated field comprises only 60% of the measured field. One also notes that the calculated field does not depend strongly[14] on the Cd 5s occupation due to the dependence of the normalization constants on a_{5s}. This means that the spin density parameters are relatively insensitive to direct metal 3d-Cd 5s transfer, which we have neglected. The oxide data previously reported[4] support this contention, since from Table IA we see that the oxide fields are all comparable, even though Lau and Newman[41] have calculated that in pure MnO direct 3d-4s transfer will dominante the transferred hyperfine interactions.

In view of the limitations inherent in using Eq. 9 to predict hyperfine fields and thus spin-density parameters, we will normalize our data to $KNiF_3$ ($f_\sigma = 3.8\%$[21]) and make estimates for other compounds relative to this reference point.

Table V. Calculated H_{hf} for $KNiF_3$ f_σ = 3.8%

	Cd 5s Occupation			Experimental Field
	0%	20%	40%	
Cd-F = 2.01 Å (Ni-F)	62 KOe	84 KOe	79 KOe	105 KOe
Cd-F = 2.15 Å ($KCdF_3$)	40 KOe	66 KOe	66 KOe	105 KOe

Sawatzky's MO formulation provides a basis for the way in which the hyperfine field is expected to scale with f_σ . Figure 6 shows the results of a calculation (using parameters appropriate to NiO) in which the Cd parameters were held fixed and f_σ allowed to vary. One can see that the functional relationship connecting f_σ to the hyperfine field is not as simple as a linear approximation, but we will show that the assumption of a linear scaling will provide a reasonable lower bound to the estimated f_σ values. NMR[21] and ENDOR[24] results are available for Ni^{2+} in fluorides and oxides, yielding f_σ = 3.8% and 8.5% respectively. By adopting the figure of 3.8% and scaling the hyperfine fields for NiO and $KNiF_3$ found in Table IA we would estimate f_σ = 7% in NiO. In Fig. 6 the calculated fields for f_σ = 4% and 8% were 55.3 and 99.7 KOe, and their ratio is 1.8 rather than the 2.0 (8%/4%) expected from the f_σ values. Thus we see that the use of a linear approximation yields estimates of order 10% low because of curvature in the H_{hf} vs f_σ curve, but that the estimate of 7% is within about 20% of the ENDOR result and will be systematically low when generated by a ratio of fields. More quantitative studies[4] have taken this curvature correction into account in order to obtain more precise values for the f_σ parameters in the oxide series. In this paper however, we are more concerned with elucidating the systematic trends in the data and will thus content ourselves with estimates which represent lower bounds.

The comparison of fluoride, oxide, chloride and sulfide measurements necessitates dropping the constraint that the Cd-ligand parameters be held fixed as they were for the field calculations of Table V. To estimate the effect of changing the Cd-ligand properties, we have

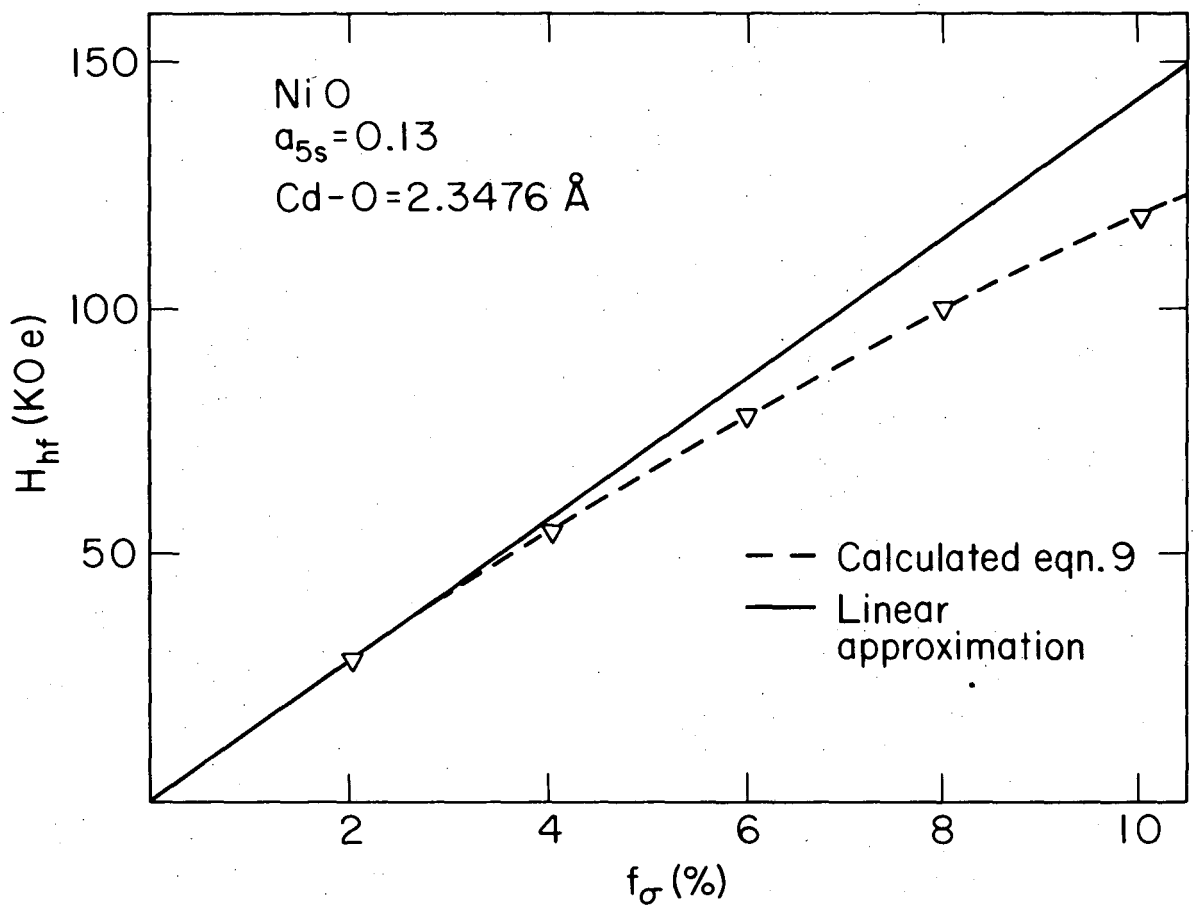

Fig. V-6.

XBL758-3698

calculated the ratio $H_{hf}(Mn\text{-}L)/H_{hf}(Mn\text{-}F)$ with f_σ held constant. The overlap integrals were those characteristic for Cd-L bond distances in the compounds $KCdF_3$, CdO, and Rb_2CdCl_4. In order to generate relative Cd 5s occupations for the various ligands, we plotted $1/R_{Cd\text{-}L}$ versus the empirical covalency parameter ($C=1-0.16\,|\chi_m-\chi_L| - 0.035|\chi_m-\chi_L|^2$) found by Hannay and Smyth,[22] and found the approximately linear relation shown in Fig. 7. (The metal and ligand electronegativities were taken from the paper of Gordy and Thomas.)[23] For $KNiF_3$, we have $f_\sigma = (\gamma + S)^2 = 3.8\%$, and a calculation of the overlap contribution yields for $\gamma_{Ni\text{-}F} \sim 0.135$. A Cd-F γ value was generated by scaling the covalency parameters for Cd-F/Ni-F. This yields $\gamma_{Cd\text{-}F} \sim 0.106$. The a_{5s} parameter was then adjusted to yield a Cd-F 5s occupancy of 10.6%. The other ligand 5s occupancies were scaled by the linear relationship of Fig. 7. The result of the calculation for f_σ fixed at 8% is

$$\frac{H_{hf}(Mn\text{-}L)}{H_{hf}(Mn\text{-}F)} = 1.0\pm0.1 \quad L = F^-,\ O^{2-},\ \text{and}\ Cl^-. \tag{11}$$

The total spread in the relative fields with f_σ held fixed is only of order 10% and indicates that the magnitude of the experimental fields are not grossly sensitive to a consistent set of Cd-ligand parameters. By a consistent set of parameters we mean Cd-ligand bond distances which are either all "long" or all "short" with their associated overlaps. Thus major changes in measured hyperfine fields are to be primarily associated in changes in f_σ and a simple ratio of measured fields should provide a reasonable lower bound to the spin density parameters.

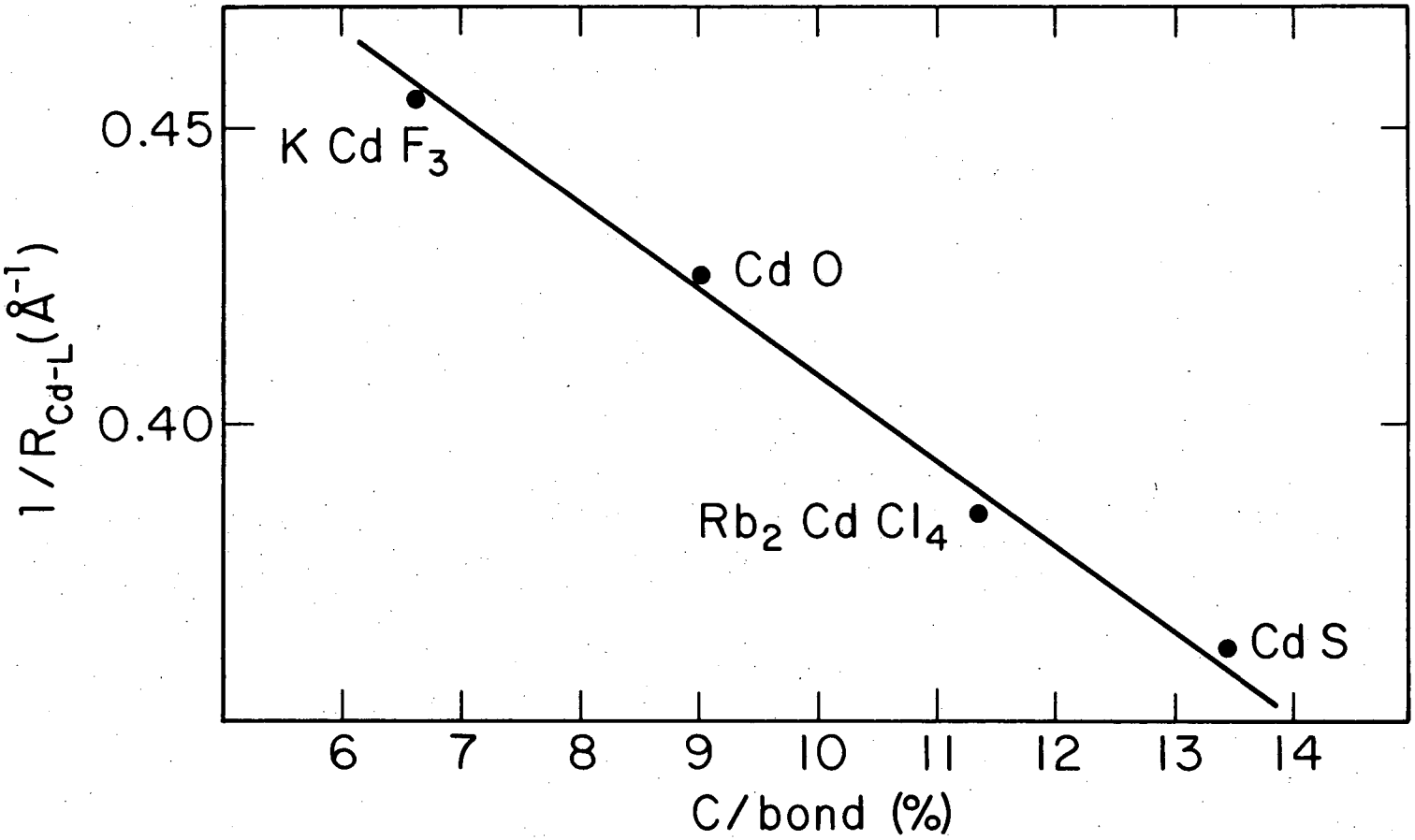

Fig. V-7.

XBL758-3693

D. SYSTEMATICS OF THE Cd HYPERFINE FIELDS AND SPIN DENSITY PARAMETERS

Before starting an analysis of the data in Tables IA and IB, it is necessary to digress and explain how the fields listed in the column H_{hf} were arrived at. The reason that the hyperfine fields differ by more than a normal dipolar contribution from the experimental values is due to zero point spin deviations in Heisenberg-like antiferromagnets.[25]

The necessity for this correction arises because of the term $\frac{\langle S_z \rangle}{S}$ (Eq. 9). The deviation of $\langle S_z \rangle$ from its full value in these high-spin complexes depends on the dimensionality of the magnetic lattice. For that reason we have separated the host materials into two- and three-dimensional categories. Note that the Co compounds K_2CoF_4 and Rb_2CoF_4 are Ising-like,[26] and should therefore not display any spin deviations. We assume that the full theoretical[25] spin deviation is present for both the magnetically two- and three-dimensional Heisenberg-like compounds. In this case

$$\left.\frac{\langle S_z \rangle}{S}\right)_{2,3} = 1 - \frac{\Delta_{2,3}}{S}, \text{ where } \Delta_2 = 0.197 \text{ and } \Delta_3 = 0.078. \quad (12)$$

Thus the spin deviations for Ni^{2+} (S=1) are much larger than for Mn^{2+} (S = 5/2) and vary with the magnetic dimensionality. The hyperfine field is then related to the experimentally measured value by

$$H_{hf} = H_{exp}/1-\Delta/S \pm H_{dip} \quad (13)$$

where an additional (and usually small) dipolar field correction has also been made whenever the relative sign of the dipolar and supertransferred fields is known.

We wish to examine the systematic trends of the hyperfine fields for Cd doped into various host antiferromagnets. We will begin by considering the effect of moving across the transition metal group for a fixed ligand. For the fluorides the data allow the following comparisons.

$KMnF_3$(124.4) $KCoF_3$(78.2)

$RbMnF_3$(117.4)→ $KFeF_3$(104.2)→ $RbCoF_3$(71.5)→$KNiF_3$(113.7)→ $KCuF_3$(<4)

$TlMnF_3$(122.5) $TlCoF_3$(71.6)

and

K_2MnF_4 (79.4) → K_2CoF_4(52.7) → K_2NiF_4(69.3)

Rb_2MnF_4(75.4) Rb_2CoF_4(50.0) Rb_2NiF_4(64.7)

Several comments are in order concerning some of the field values. Of particular interest are the consistently low Co^{2+} values, which we attribute to the fact that the orbital angular momentum is not quenched in these compounds. This is also expected to be present to some degree in the Fe^{2+} compound, but the effective reduction of the spin expectation value is clearly not as large. In addition, $KMnF_3$[27,28] and $KFeF_3$[29] both have lattice distortions and canted spin structures at liquid helium temperatures. The field for $KMnF_3$ is a rough estimate based on assuming that

$$H_{hf}(KMnF_3) = \frac{H_{hf}(K_2MnF_4)}{H_{hf}(Rb_2MnF_4)} \times H_{hf}(RbMnF_3) = 124.4\text{KOe}.$$

No attempt was made to estimate a field for "uncanted" $KFeF_3$. The hyperfine fields for these compounds should therefore be considered as only approximate.

The $KCuF_3$ is a special case which reflects the strong Jahn-Teller effect and the A type magnetic structure of the compound. The Jahn-Teller effect leads to an orthorhombic distortion of the $(CuF_6)^{4-}$ octahedron with two short and two long Cu-F bonds in the (001) plane and a medium Cu-F separation for the two anions along the c-axis[30] (see Fig. 8). The Cu^{2+} ground state (x^2-y^2) and F^- $2p\sigma$ wavefunctions are arranged such that in the (001) plane unpaired spin is approximately transferred only from the two neighboring magnetic ions along the c-axis and from the Cu's with short Cu-F bonds. Spins in adjacent (001) planes are coupled antiferromagnetically however, so that the transferred spin densities are antiparallel and expected to cancel at the Cd nucleus. This is consistent with our observation that $H_{hf} \leq$ 4KOe.

The general trend in the fluorides with perovskite or perovskite-like structures in moving across the 3d metal group is that the fields are very nearly equal in magnitude, with the Co values systematically low. The same trends are present for the oxide series with NaCl structure,

$$MnO(208) \rightarrow CoO(187) \rightarrow NiO(212).$$

The virtual constancy of the fields for a fixed ligand and crystal structure is expected on a chemical basis. The electron affinities for the 3d transition metals are comparable (Mn^{2+} is slightly low) and the bond distances are quite similar. Thus one expects that the spin density parameter f_σ, which has both covalent and overlap components, will not alter drastically across the transition metal group under the constraint of fixed ligand and crystal structure. In order to estimate spin density parameters for our data, we will make the assumption outlined in

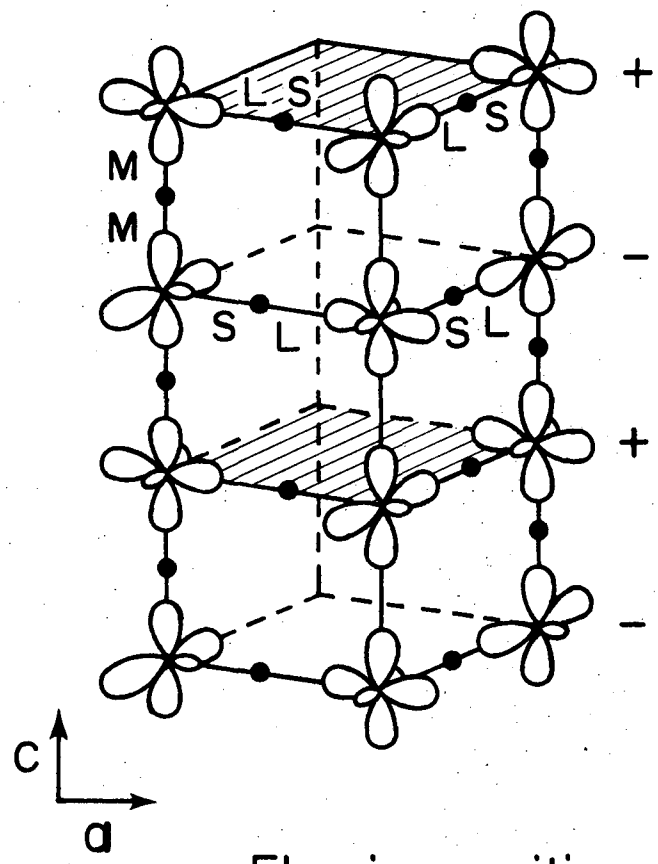

Fig. V-8.

Section III that f_σ scales linearly with H_{hf}, and will use the value for $KNiF_3$ (f_σ = 3.8%) as a normalization point. The compounds of form A_2MX_4 have only 4 magnetic spins contributing to the transferred Cd field, so that field value for $KNiF_3$ (113.7 KOe) was reduced by 4/6 before making a spin-density estimate. The f_σ results for our PAC data are shown in Table 6, along with results of other techniques.

A few additional points concerning the PAC estimated fluoride and oxide spin density parameters are worth noting. First of all, Mn^{2+} does not appear to be anomalous in either fluoride or oxide series. Particularly in the fluorides, a value of approximately 4% is consistent with the basic trend that the expected order of magnitude is 3-5%. Even though our estimate for NiO is lower by 20% than the ENDOR result, the near constancy of the measured fields indicates that the oxides, like the fluorides, have essentially similar f_σ values. We thus feel that a lower bound of 7% for MnO is quite reasonable and contend that nothing anomalous happens in passing along the 3d group metals in isomorphous salts. Based on our normalization to NMR fluoride data, the reasonable agreement with the ENDOR measurement for Ni^{2+} (MgO) argues for the basic equivalence of data measured in diluted and concentrated magnetic systems. The Co data consistently show the effects of unquenched orbital angular momentum in all the various techniques.

We now turn to the trends expected when the 3d metal is held fixed and the ligands varied. Only Mn compounds exist in magnetic structures which can be compared for all the ligands F^-, O^{2-}, Cl^-, and S^{2-}. In order to incorporate all four ligands it is necessary to use data from the quadratic-layer compounds to obtain a chloride value. The equivalence

Table 6. f_σ values derived from PAC

Mn^{2+}	Fe^{2+}	Co^{2+}	Ni^{2+}
PAC (f_σ)	PAC (f_σ)	PAC (f_σ)	PAC (f_σ)
4.2% ($KMnF_3$)	3.5% ($KFeF_3$)	2.6% ($KCoF_3$)	3.8% ($KNiF_3$)
3.9% ($RbMnF_3$)		2.4% ($RbCoF_3$)	3.5% (K_2NiF_4)
4.1% ($TlMnF_3$)		2.4% ($TlCoF_3$)	3.2% (Rb_2NiF_4)
4.0% (K_2MnF_4)		2.6% (K_2CoF_4)	
3.8% (Rb_2MnF_4)		2.5% (Rb_2CoF_4)	
NMR/ESR ($f_\sigma - f_\pi$)		ESR $\left(\frac{f_\sigma + f_\pi}{2}\right)$	NMR/ESR (f_σ)
0.2% ($KMnF_3$)[a]			3.8% ($KNiF_3$)[e]
0.3% ($RbMnF_3$)[b]		2.4% ($KMgF_3$)[d]	3.2% ($KMgF_3$)[f]
0.3% ($KMgF_3$)[c]		assume $f_\sigma \sim f_\pi$	
		estimate $f_\sigma \sim 2.4\%$	ND ($f_\sigma + f_s$)
			25% ($KNiF_3$)[g]
			$f_s \sim 0.5\%$
			estimate $f_\sigma \sim 2.1\%$

Oxides

PAC (f_σ)		PAC (f_σ)	PAC (f_σ)
7.0% (MnO)		6.2% (CoO)	7.1% (NiO)
ND($f_\sigma + 2f_\sigma + f_s$)[h]			ENDOR (f_σ)
3.6% (MnO)			8.5% (MgO)[j]
$f_\sigma \sim f_\pi$, $f_s \sim 0.6$			
estimate $f_\sigma \sim 1.5\%$			ND ($f_\sigma + f_s$)[k]
			3.8% (NiO)
ENDOR ($f_\sigma - f_\pi$)[i]			$f_s \sim 0.7\%$
0.8% (MgO)			estimate $f_\sigma \sim 3.1\%$

Chlorides

PAC (f_σ)	ESR $\frac{(f_\sigma + f_\pi)}{2}$
5.4% (Rb_2MnCl_4)	5%($CoCl_6$)$^{-4}$

Sulfides

PAC (f_σ)
8.6% (α-MnS)
ND($f_\sigma + 2f_\pi + f_s$)
7.0% (α-MnS)[m]
estimate $f_\sigma \sim 3.1\%$

[a]Ref. 21 [b]Ref. 31 [c]Ref. 32 [d]Ref. 33 [e]Ref. 21 [f]Ref. 32 [g]Ref. 34

[h]Ref. 35 [i]Ref. 36 [j]Ref. 24 [k]Ref. 37 [l]Ref. 12 [m]Ref. 37

of f_σ values between the perovskites and quadratic-layer compounds $KMnF_3/K_2MnF_4$, $RbMnF_3/Rb_2MnF_4$, $KCoF_3/K_2CoF_4$, $RbCoF_3/Rb_2CoF_4$ and $KNiF_3/K_2NiF_4$ when adjustments for spin deviations and number of magnetic neighbors are made illustrates that the quadratic-layer compounds yield f_σ estimates consistent with a perovskite-like magnetic sublattice. The hyperfine fields in MnO and MnS also derive from a perovskite-like magnetic lattice[4] so we will consider the series Rb_2MnF_4, MnO, Rb_2MnCl_4 and MnS.

One expects a weak dependence on the Cd-ligand parameters and a systematic increase in observed hyperfine field on traversing the series F^-, O^{2-}, Cl^- and S^{2-} in the direction of increasing covalency. Table VII shows that the measured fields for the chalcogenides MnO and MnS and their derived spin density parameters are not consistent with this trend. We suggest that the answer is reflected in the graph of Fig. 9, in which we have separated the halides and the chalcogenides and plotted the derived f_σ values versus the covalency parameter of Hannay and Smyth.[22] For all four compounds the magnetic sublattice contributing to the observed fields are equivalent, but there is a decided difference between the perovskite-like K_2NiF_4 structure and the NaCl structure of MnO and MnS. In the first case the fluoride and chloride ligands are coordinated to only two magnetic neighbors (pure host) while in the NaCl structure the ligands are attached to six magnetic neighbors. The spin structure in MnO and MnS is such that most of these moments cancel at a Cd impurity by symmetry,[4] but the charge pulling effect on the ligand is still present. We suggest that this is the reason why the

Table VII

Magnetic Host	H_{hf} (KOe)	f_{σ} (%)
Rb_2MnF_4	115	3.8%
Rb_2MnCl_4	160	5.4%
MnO	208	7.0%
α-MnS	258	8.6%

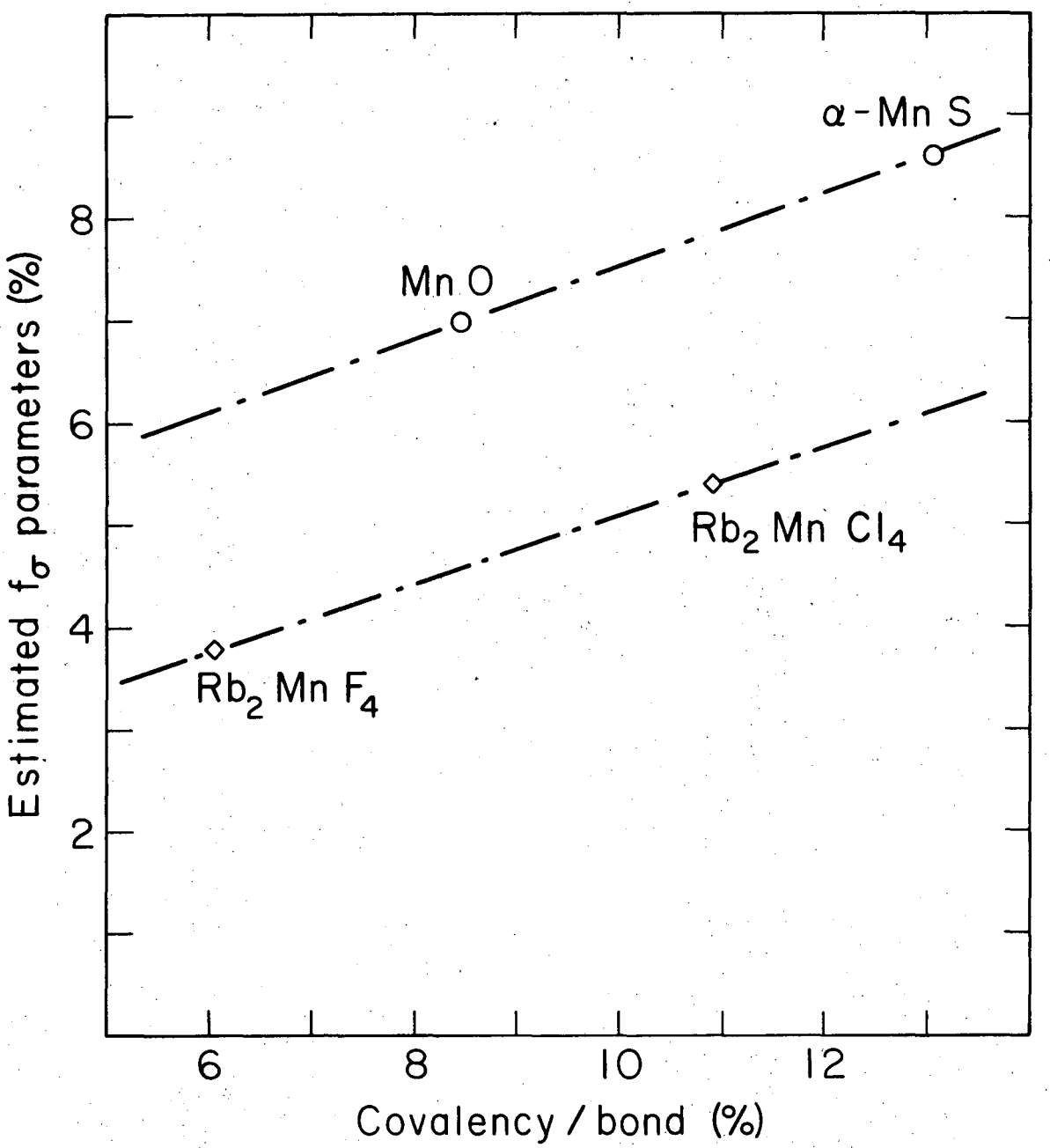

Fig. V-9.

XBL 758-3692

chalcogenides have fields of order 200-250 KOe and the "adjusted" quadratic-layer halides fields of 120-160 KOe. Even though only two points exist on each "curve", we feel that the plot of Fig. 9 is fairly indicative of the anticipated increase in f_σ due to increasing anion covalency.

E. CONCLUSION

We have applied a simple model to the estimation of spin density parameters derived from PAC data and find the expected systematic trends both along a group and down a column. The data indicate that spin density parameters derived from concentrated and dilute samples are approximately equal, and that increasing ligand covalency is reflected in increasing values of the spin density parameters. We also conclude that Mn does not act anomalously in either in fluoride or oxide series and we estimate f_σ values for Mn^{2+} in the perovskite-like fluorides of 4% and values of order 7-8% for the oxides.

REFERENCES

1. J. B. Goodenough and J. M. Longo Landolt-Bornstein III/4a, Magnetic Oxides and Related Compounds
Springer-Verlag, Berlin-Heidelberg-
New York 1970 p: 126-275.

2. H. H. Rinneberg and D. A. Shirley ($RbMnF_3$ paper) Phys. Rev. Lett. 30 (22), 1147 (1973).

3. H. Haas and D. A. Shirley, LBL-1284 (1972). Submitted to Journal of Chemical Physics.

4. H. H. Rinneberg and D. A. Shirley (NiO paper) LBL-2900 (1974). Submitted to Phys. Rev. B.

5. B. Erik Karlsson, Arkiv. Fysik 22, 1 (1962).

6. Handbook of Preparative Inorganic Chemistry V2, Edited by Georg Brauer, p. 1465, Academic Press, New York, London 1965.

7. Perturbed Angular Correlations, Edited by E. Karlsson, E. Mathias, and K. Siegbahn, North Holland Pub. Co.-Amsterdan (1964).

8. H. H. Rinneberg and D. A. Shirley - difluoride paper, LBL-2398 (1974). Submitted to Phys. Rev. B.

9. J. H. Van Vleck, Phys. Rev. 41, 208 (1932).

10. J. S. Griffith "The Theory of Transition Metal Ions" Cambridge University Press, London (1961).

11. C. J. Ballhausen "Introduction to Ligand Field Theory" McGraw-Hill, New York (1962).

12. J. Owen and J. H. M. Thornley, Rep. Prog. Phys. 29, 675 (1966).

13. J. A. Tossel, D. J. Vaughan and K. H. Johnson Nature 244, 42 (1973).

14. F. van der Woude and G. A. Sawatzky, Phys. Rev. B. 4(9) 3159 (1971).

15. J. M. D. Cocy and G. A. Sawatzky, J. Phys. C: Solid St. Phys. 4, 2386 (1971).

16. C. Boekema, F. van der Woude, and G. A. Sawatzky, Int. J. Magnetism 3, 341 (1972).

17. J. B. Mann, Los Alamos Sci. Lab. Report LA-3691 (1968).

18. E. Clementi, IBM J. Res. Developm. 9, 2 (1965).

19. J. Yamashita and S. Asano, J. Phys. Soc. Japan 28, 1143 (1970).

20. Y. Toyotomi and R. Onaka, J. Phys. Soc. Japan 34, 623 (1973).

21. R. G. Shulman and K. Knox, Phys. Rev. Lett. 4, 603 (1960).

22. N. B. Hannay and C. P. Smyth, J. Am. Chem. Soc. 68, 171 (1946).

23. W. Gordy and W. J. O. Thomas, J. Chem. Physics 24, 439 (1956).

24. P. Freund, J. Phys. C: Solid State Phys. 7, L33 (1974).

25. P. W. Anderson, Phys. Rev. 86, 694 (1952).

26. D. J. Breed, K. Gilijamse, and A. R. Miedema, Physica 45, 205 (1969).

27. A. J. Heeger, O.Beckman,, and A. M. Portis, Phys. Rev. 123, 1652 (1961).

28. K. Saiki, K. Horai, and H. Yoshioka, J. Phys. Soc. Japan 35, 1016 (1973).

29. G. R. Davidson, M. Eibschütz, and H. J. Guggenheim, Phys. Rev. B 8, 1864 (1973).

30. S. Kadota, I. Yamada, S. Yoneyama, and K. Hirakawa, J. Phys. Soc. Japan 23, 751 (1967).

31. M. B. Walker and R. W. H. Stevenson, Proc. Phys. Soc. 87, 35 (1966).

32. T. P. P. Hall, W. Hayes, R. W. H. Stevenson, and J. Wilkens, J. Chem. Phys. 38, 1977 (1963), 39, 35 (1963).

33. J. H. M. Thornley, C. G. Windsor, and J. Owen, Proc. Roy. Soc. A 284, 252 (1965).

34. M. T. Hutchings and H. J. Guggenheim, J. Phys. C: Solid State Phys. 3, 1303 (1970).

35. A. J. Jacobson, B. C. Tofield, and B. E. F. Fender, J. Phys. C: Solid State Phys. 6, 1615 (1973).

36. P. Freund, J. Owen, and B. Hann, J. Phys. C: Solid State Phys. 6, L139 (1973).

37. B. E. F. Fender, A. J. Jacobson, and F. A. Wedgwood, J. Chem. Phys. 48, 990 (1968).

38. CRC Handbook of Chemistry and Physics 53rd Edition, B202, 1972-1973. Chemical Rubber Company, Cleveland, 1972, R. C. Weast, Ed.

39. R. E. Watson, Phys. Rev. 111, 1108 (1958).

40. S. Huzinaga and A. Hart-Davis, Phys. Rev.Annal 8, 1734 (1973).

41. B. F. Lau and D. J. Newman, J. Phys. C: Solid State Phys. 6, 3245 (1973).

FIGURE CAPTIONS

Fig. 1. Time modulated perturbation factor for ^{111m}Cd in $KCuF_3$ illustrating the effect of a non-zero asymmetry parameter on the periodicity of the oscillations. The time calibration is 1.619 ns/channel.

Fig. 2. Time spectrum for ^{111m}Cd in K_2NiF_4 at 4.2°K which displays the effects of a combined magnetic dipole-electric quadrupole interaction. The time calibration is 1.619 ns/channel.

Fig. 3. Power spectral density transform of the combined interaction time spectrum of ^{111m}Cd in K_2NiF_4 at 4.2°K.

Fig. 4. Molecular orbital diagram for the 3d transition metal salts.

Fig. 5. Schematic diagram of the extended octahedral complex relative to Cd-doped host antiferromagnets with perovskite-like magnetic structures.

Fig. 6. Plot of calculated hyperfine fields based on the extended cluster model versus spin density. The Cd parameters have been held fixed in this calculation.

Fig. 7. Plot of $1/R_{Cd\text{-}Ligand}$ versus the Cd-Ligand covalency/bond as defined by Hannay and Smyth.

Fig. 8. Crystallographic and spin structure of $KCuF_3$ showing the half-filled Cu orbitals after Ref. 30. Another crystallographic modification exists.

Fig. 9. Plot of our estimated spin density parameters versus the Mn-Ligand covalency. Two separate anticipated trends are shown for the chalcogenides (NaCl structure) and the halides (perovskite-like structure).

VI. MEASUREMENTS OF SOLID STATE PHENOMENA*

A. Measurement of Spin Deviations, Pressure Induced Hyperfine Field Shifts; and Sublattice Magnetizations Using Perturbed Angular Correlations

1. Introduction

TDPAC studies of metals and alloys have proliferated in recent years following the resurgence of theoretical interest in the electric field gradients of pure metals. Applications in insulators remain minimal however, and have not tended to emphasize the fundamental properties of solids which are potentially available through measurements of magnetic and electric hyperfine interactions.

The purpose of this paper is to demonstrate that in a manner analogous to resonance methods, PAC techniques can be applied to probe a versatile range of solid state phenomena. Apropos to this endeavor, we have measured the deviation of the spin expectation value in magnetically two-dimensional Heisenberg-like antiferromagnets induced by quantum mechanical zero-point energy as well as the sublattice magnetization next to a diamagnetic impurity. Finally we report the first PAC measurements in an insulator of the pressure induced shift of the supertransferred hyperfine field in Cd-doped α-MnS. Section 2 contains the experimental details, while Sections 3 and 4 treat the results and discussion of these experiments.

2. Experimental

a) Sample Preparation

The preparation of Cd-doped MnF_2[1], $RbMnF_3$[2], $KNiF_3$[2], and K_2NiF_4[3],

---

*This section of work was done in conjunction with H. H. Rinneberg and D. A. Shirley.

Rb_2MnF_4[3], and α-MnS[3] has previously been reported. The basic technique involves the thermal diffusion of active $^{111m}CdF_2$ into materials prepared according to the solid state reactions

$$AX + MX_2 \xrightarrow{\Delta} AMX_3,$$

$$2AX + MX_2 \xrightarrow{\Delta} A_2MX_4. \qquad (1)$$

Since KF and RbF are both highly hygroscopic, it was necessary to work under dry conditions both in the preparation and doping of compounds reacted in the solid state.

Active α-MnS was prepared by coprecipitation, dried, and then fired to 1000 °C under a stream of dry H_2S. The concentration of Cd dopant generally did not exceed 0.1 at .% in any of the compounds.

b) Equipment and Data Analysis

The measurements of PAC spectra taken on an 8 counter γ-γ spectrometer and the subsequent data analysis are described in an earlier paper.[3]

Spectra taken at liquid helium or liquid nitrogen temperatures were obtained by immersing an aluminum sample holder directly into the refrigerant. For intermediate temperatures a regulator of the type described by Welber et al.[4] was used. The temperature was measured using a Au(Fe)/Fe thermocuple which had been calibrated against a doped germanium thermometer. A stability of ± 0.2 °K in regulation was achieved over several hours for temperatures between 15 and 100 °K.

The pressure cell employed in this work is similar to that described by S. D. Bader[5] except that the cell body was made out of A286 steel and four windows were partially machined through the body for easy γ-ray exit.

3. Results

Time spectra recorded for Cd-doped α-MnS are shown in Fig. 3. Characteristic spectra for perovskites[2] ($KNiF_3$, $RbMnF_3$), quadratic-layered fluorides[3] (K_2NiF_4, Rb_2MnF_4), and difluorides[1] (MnF_2) have previously been published. The modulation patterns have been corrected for background and exponential nuclear decay, and all samples displayed structure consistent with single phase random polycrystals. Damping in α-MnS under pressure was accounted for in the least squares fitting routine by introducing a Gaussian distribution of fields.

Table I summarizes the data relevant to the spin expectation value experiments while Tables II A,B and III list the measured parameters for the temperature dependent sublattice magnetization and pressure induced field shift studies.

4. Discussion

a) Zero point spin deviations

The problem of how the inclusion of quantum mechanical zero point energy affects the antiferromagnetic ground state was treated as early as 1952 by P. W. Anderson.[6] At that time he derived values for the expected spin deviation within the framework of spin wave theory and neglecting magnetic anisotropy. Of fundamental importance was the result that the expected magnitude of the spin deviation depended very strongly on the magnetic dimensionality of the lattice.

Considerable additional theoretical work[7,8,9] has been done on this problem, but experimental confirmation was lacking until the late 1960's when it was recognized that K_2NiF_4 and K_2MnF_4 (and their Rb analogs)

Table I.

Host	T_N (°K)	Meas. H (4.2°K) (KOe)	$\nu_Q \equiv \frac{3e^2qQ}{20\ h}$ (MHz)
$KNiF_3$	~ 253	104.8±1.5	0.0
$RbMnF_3$	82.9	113.8±1.5	0.0
K_2NiF_4	97	54.9±1.5	3.7±0.2
Rb_2MnF_4	38.5	67.9±1.5	4.7±0.2

Table II.A.

MnF_2

T_n = 66.9 °K

ν_Q = 16.5 MHz

η = 0.06

T (°K ± 0.2)	H_{exp} (KOe ± 1.5)
4.2	34.0
16.5	33.3
21.0	32.3
27.4	31.5
32.1	29.6
37.0	28.3
40.3	27.1
45.2	25.2
50.3	23.0
56.9	18.8
61.5	14.6

Table II.B.

$RbMnF_3$

$T_n = 82.9°K$

$\nu_Q = \eta = 0$

T (°K ± 0.2)	H_{exp} (KOe ± 1.5)
4.2	113.8
17.0	111.8
30.0	104.6
40.0	97.5
50.0	87.3
60.0	75.0
66.0	65.8
72.0	51.0
77.0	39.8

Table III.

α-MnS T_N = 156°K

$\nu_Q = \eta = 0$

Host	Pressure	H_{exp} (KOe)
α-MnS	1 bar	244.4 ± 2.0
α-MnS	20 kbar ± 4 kbar	253.6 ± 2.0

represented to a very good approximation two-dimensional quadratic-layer antiferromagnets. Figure 1 shows why this is so. K_2NiF_4 is made up of magnetic planes which are the same as those of $KNiF_3$ except that along the c axis a layer of KF separates the next magnetic plane, whose spins cancel by symmetry at the central ion site. In performing nuclear Cd-doped experiments in these compounds and in $KNiF_3$, the field at the Cd is generated by four magnetic neighbors of the same sublattice in the two-dimensional materials and by six in the three dimensional $KNiF_3$. In the central magnetic plane of K_2NiF_4 the bond length (Ni-F) is 2.003 Å,[10] very close to the Ni-F bond in $KNiF_3$, 2.007 Å.[10] Furthermore, the anisotropic part of the hyperfine structure constant (A) which measures the unpaired spin density in the F^- ($2p_\sigma$) orbitals has been determined from ^{19}F NMR and found to agree within the experimental limits ($A_\sigma(KNiF_3) = 8.8\times10^{-4}$ cm^{-1}, Ref. 11; $A_\sigma(K_2NiF_4) = 9.15 \pm 0.5\times10^{-4}$ cm^{-1}, Ref. 12).

We shall therefore assume that the supertransferred Cd hyperfine field per nearest magnetic neighbor, H_0, is equal in the two compounds. Using our data for $KNiF_3/K_2NiF_4$ and $RbMnF_3/Rb_2MnF_4$ we will now estimate the spin deviation in the two dimensional structures.

Taking n = 2,3 to define the magnetic dimensionality, we describe the supertransferred hyperfine field at the Cd nucleus by

$$H_n^{meas} = Z_n \cdot \left\langle \frac{S_z}{S} \right\rangle_n \cdot H_0 \qquad (1)$$

where Z_n is the number of magnetic ions contributing to the field and

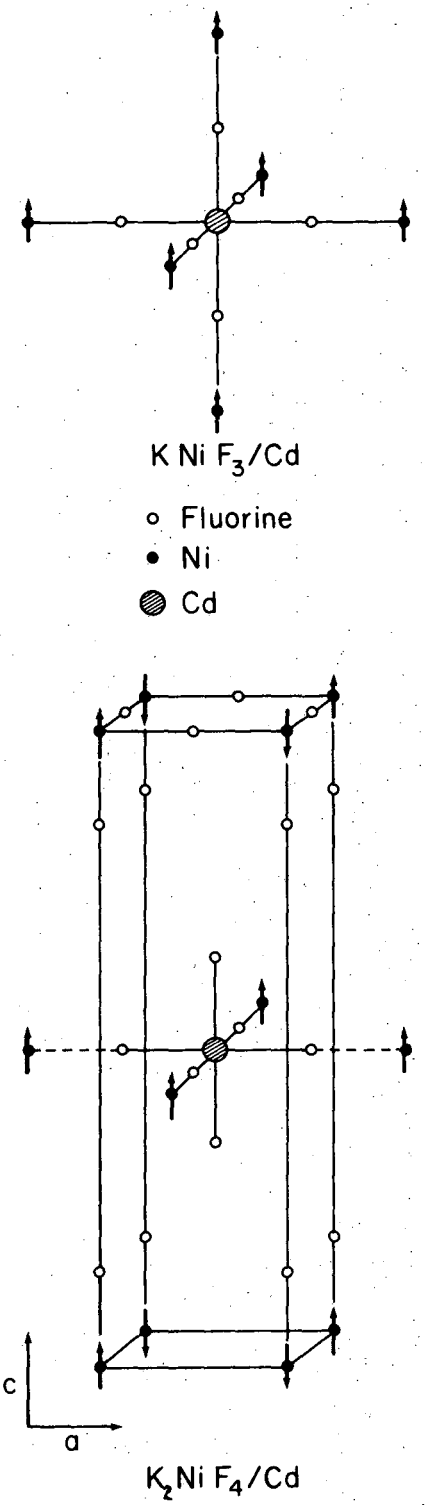

Fig. VI-1.

$$\left\langle \frac{S_z}{S} \right\rangle_n = 1 - \frac{\Delta_n}{S} \quad .$$

For $Z_2 = 4$ and $Z_3 = 6$ it follows that

$$\Delta_2 = S \left\{ 1 - \frac{H_2^{meas}}{H_3^{meas}} \cdot \frac{6}{4} \left(1 - \frac{\Delta_3}{S} \right) \right\} \qquad (2)$$

In this expression the measured hyperfine fields for the two-dimensional antiferromagnets K_2NiF_4 and Rb_2MnF_4 have to be corrected for dipolar fields[13] of 1.3 and 2.5 KOe respectively.

Although the zero point spin deviation in a three-dimensional Heisenberg antiferromagnet has not yet been unambiguously resolved, we will assume the value predicted by spin wave theory[6] (without anisotropy correction) which gives $\Delta_3 = 0.078$.

Using the experimental field values of Table I (corrected where necessary for dipolar fields) and S = 1, 5/2 for Ni^{2+} and Mn^{2+} respectively, we obtain the following estimates from our PAC data

$$\Delta_2(K_2NiF_4) \sim 0.26$$

$$\Delta_2(Rb_2MnF_4) \sim 0.25.$$

Spin-wave formalism yields a theoretical value[6] for Δ_2 of 0.197 (uncorrected for anisotropy). Lines[8] has calculated the effect of finite anisotropy which can be combined with the anisotropy fields measured by susceptibilities and AFMR to give $\Delta_2(K_2NiF_4) = 0.18$ and $\Delta_2(Rb_2MnF_4) = 0.167$. These values are in excellent agreement with recent experimental ENDOR[14] and NMR[13] studies which gave 0.20 (K_2NiF_4) and 0.17 (Rb_2MnF_4).

Our estimates of 0.25-0.26 are high but not unreasonable in view of the fact that Eq. 1 is a rather drastic approximation for describing the supertransferred hyperfine field at the Cd nucleus.

b) Temperature Dependent Sublattice Magnetization

The temperature dependence of the Cd fields in $RbMnF_3$ and MnF_2 is shown in Fig. 2. For comparison we include the MFA Brillouin function of S = 5/2 and the temperature dependence of the sublattice magnetization in MnF_2 as measured by ^{19}F NMR.[15] $RbMnF_3$ has the simple perovskite structure of Fig. 1 with six nearest magnetic neighbors which belong to the same sublattice. In MnF_2 the field at the impurity has to be corrected for a dipolar contribution[15] (5.8 KOe at 4.2°K) to obtain the supertransferred hyperfine field. For MnF_2, the unpaired spin density in the Cd s shells is caused by two nearest magnetic neighbors of one sublattice and eight next nearest Mn^{2+} belonging to the other sublattice, with the latter probably dominating. Although the relative sign of the dipolar and hyperfine fields is not known, the dipolar field is at most a 20% correction and is expected to have the same temperature dependence as the hyperfine field. For pure MnF_2 the exchange integral of next-nearest-neighbors is much larger than the nearest-neighbor exchange constant, and the replacement of a Mn ion by the diamagnetic impurity is expected to demagnetize the second nearest neighbors so that the internal field would decrease faster with increasing temperature than the host magnetization. Although the error of the experimentally determined field in MnF_2 is large due to the presence of the quadrupole interaction, the ratio H(T)/H(0) is seen in Fig. 2 to lie systematically below the corresponding ratio for the host magnetization.

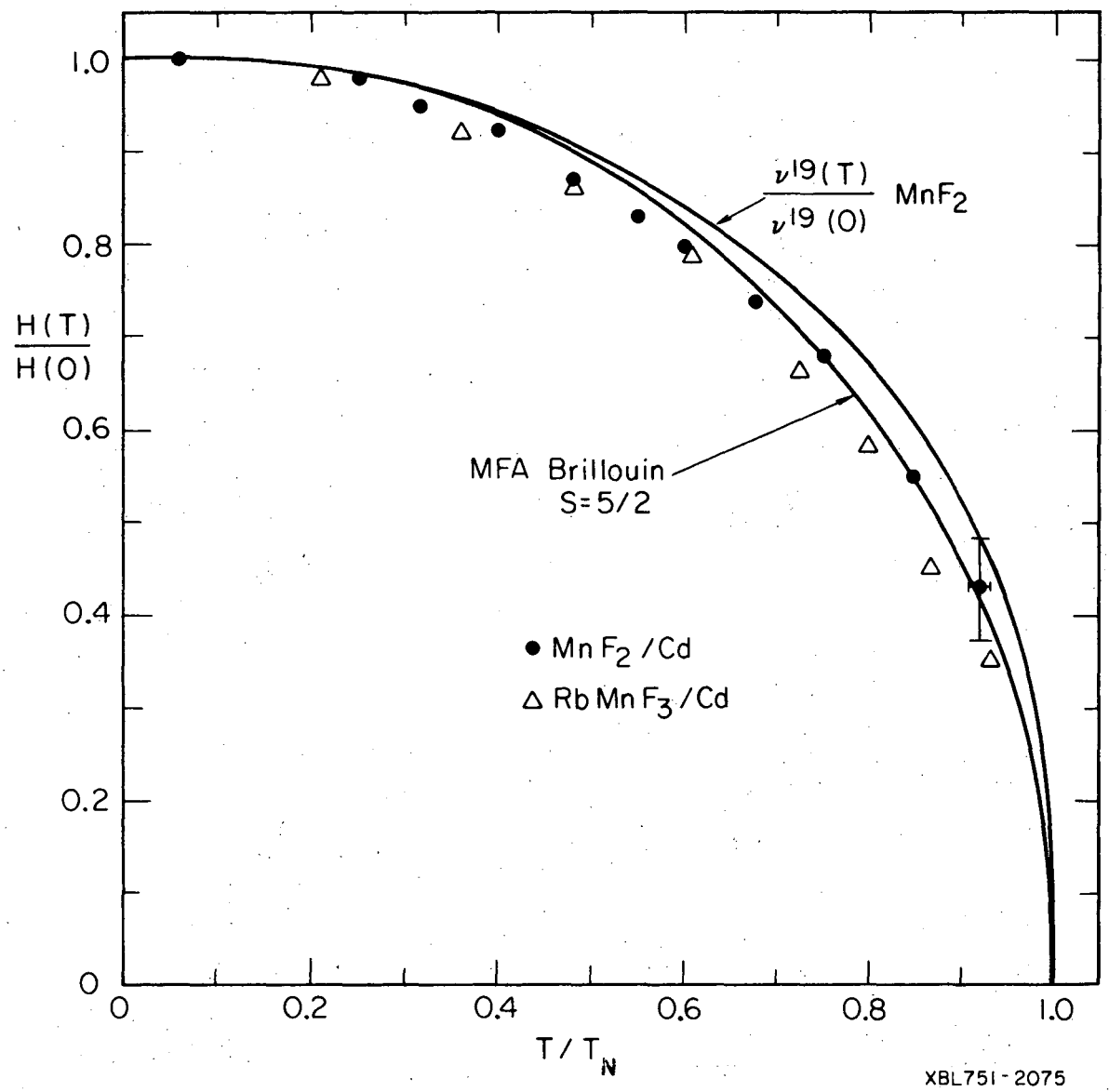
1.0
0.8
0.6
0.4
0.2
0
H(T)/H(0)
0
0.2
0.4
0.6
0.8
1.0
T / T_N
ν19(T)/ν19(0) MnF2
MFA Brillouin S=5/2
● Mn F2 /Cd
△ Rb Mn F3 /Cd
XBL751-2075

Fig. VI-A.2.

In $RbMnF_3$ the impurity demagnetizes the first nearest magnetic sublattice and the use of a reduced field/reduced temperature plot shows that the effect is comparable to that found in MnF_2.

Lovesey and Marshall[16] have performed numerical calculations of the moment reduction at the first neighbors of a diamagnetic impurity in the molecular field approximation. The calculations were done for face-centered and body-centered lattices and their results for S = 5/2 with either lattice decrease more rapidly with increasing temperature than our experimental data.

c) Pressure Induced Shift of the Supertransferred Field of Cd in α-MnS

In a magnetic insulator the origin of the field at the doped diamagnetic Cd site arises through overlap and covalency effects with transfer of unpaired spin density from the magnetic ions through the intervening ligands and into the s shells of Cd. In an insulator these overlap and covalency effects are short range, and thus the pressure dependence of H_{hf}(Cd) relates critically to the bond distances and thus the relative size of the two effects.

In order to estimate the expected shift in α-MnS we will use a highly abbreviated model which scales H_{hf}(Cd) proportional to $f_\sigma \langle L|Cd\ ns\rangle^2$, where f_σ is the unpaired spin density transferred from the magnetic ion to the ligand and $\langle L|Cd\ ns\rangle$ represents the overlap between the ligand orbitals and the cadmium ns shells. The ligand orbitals of primary interest would be the S^{2-} $3p_\sigma$ wavefunctions, which are unfortunately not available even in free-ion form. Thus we shall make an estimate which uses only the pressure dependence of f_σ, yielding

$\Delta H_{hf}(Cd)/H_{hf}(Cd) \cong \Delta f_\sigma/f_\sigma$. We also assume the kinetic model[15] for superexchange which connects J_2, the interlattice exchange constant, to f_σ by the relation:

$$J_2 \propto 2f_\pi^2 + f_\sigma^2 + f_s^2 .$$

The subscripts π, σ, and s relate to the nature of the metal-ligand bond. Available data for MnF_2[17] and MnO[18] indicate that f_π and f_σ are approximately equal, and that $f_\pi^2, f_\sigma^2 >> f_s^2$. We will assume the same for MnS and replace J_2 with $3f^2$. Our estimate for $\Delta H_{hf}(Cd)/H_{hf}(Cd)$ is now approximated by $(1/2)\Delta J_2/J_2$. One can now use the molecular field approximation, in which J_2 is proportional to T_N and the known[19] pressure dependence of T_N^{-1} $(\partial T_N/\partial p) = 8\times10^{-6}\text{bar}^{-1}$ to estimate a relative shift in the hyperfine field of 8% for Δp = 20 kbar. This represents an upper limit because the compressibility of MnS will decrease between the Néel point where $T_N^{-1}(\partial T_N/\partial p)$ is measured and 4.2°K, where the data were taken. The observed increase in field in Fig. 3 from 244.4 kOe at 1 bar to 253.6 kOe at 20 ± 4 kbar corresponds to a relative shift of $\Delta H_{hf}(Cd)/H_{hf}(Cd)$ of + 3.8 ± 0.8%. Most of the error in the field shift is associated with the pressure calibration, which was accomplished by measuring the frequency shift of ^{111}In in Cd metal and comparing the shift of Raghaven et al.[20]

We also tried to perform these pressure experiments on $RbMnF_3$, $KNiF_3$, and NiO for which we have calculated the Cd-ligand overlap integrals. We found however, that the damping of the spectra for these compounds was both severe and irreversible, and we were unable to extract meaningful field shifts.

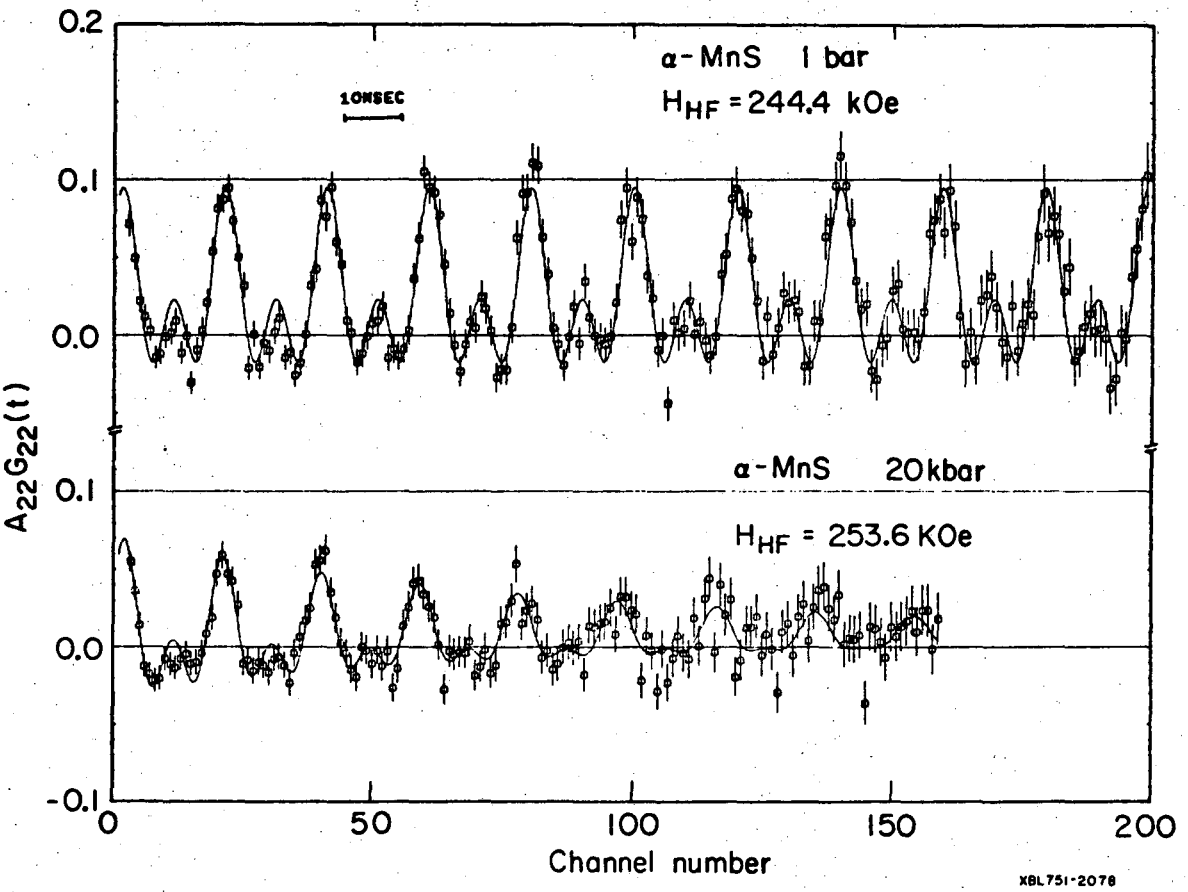

Fig. VI-A.3.

5. Summary

The measurements presented in this paper illustrate the application of PAC methods to the study of solid state phenomena in insulators. We have presented an estimate for the reduction in the spin expectation value due to quantum mechanical zero-point motion which is in fair agreement with NMR, susceptibility, and ENDOR results. Additionally we have shown that temperature dependent sublattice magnetizations and pressure induced supertransferred hyperfine field shifts can be measured using the technique of perturbed angular correlations. A wide variety of solid state properties still remain to be explored in the near future.

ACKNOWLEDGMENTS

We thank Duane Newhart for valuable assistance in both the design and construction of the pressure cell. We also wish to acknowledge several helpful discussions with Drs. S. D. Bader, G. Kaindl, and R. Schock.

REFERENCES

1. H. H. Rinneberg and D. A. Shirley Phys. Rev. B 11, 248 (1975).

2. H. H. Rinneberg and D. A. Shirley, Phys. Rev. Lett. 30, 1147 (1973).

3. H. H. Rinneberg, G.P.Schwartz and D. A. Shirley *Companion Paper - submitted to Hyperfine Interactions.

4. B. Welber and E.E. Tynan , Rev. Sci. Instrum. 38, 137 (1967).

5. S. D. Bader, Thesis, University of California, Berkeley, January 1974, LBL-2297.

6. P. W. Anderson Phys. Rev. 86, 694 (1952).

7. H. L. Davis, Phys. Rev. 120, 789 (1960).

8. M. E. Lines, J. Phys. Chem. Solids 31, 101 (1970).

9. J. H. Y. Colpa, E. G. Sieverts, R. H. van der Linde, Physica 51, 573 (1971).

10. Landolt Börnstein III/7a, Ed. K.-H. Hellwege, Springer Verlag Berlin-Heidelberg-New York, 1973).

11. R. G. Shulman and S. Sugano, Phys. Rev. 130, 506 (1963).

12. E. P. Maarschall, A. C. Botterman, S. Vega, and A. R. Miedema, Physica 41, 473 (1969).

13. H. W.de Wijn , L. R. Walker, and R. E. Walstedt, Phys. Rev. B8, 285 (1973).

14. A. H. M. Schrama, Physica 68, 279 (1973).

15. V. Jaccarino in Magnetism V3A, p. 331, Ed. G. R. Rado and H. Suhl, Academic Press, New York, London 1965.

16. S. W. Lovesey and W. Marshall, Proc. Phys. Soc. 89, 613 (1966).

17. J. Owen and J. H. M. Thornley, Repts. Progr. Phys. 29, 675 (1966).

18. P. Freund, J. Owen, and B. F. Hahn, J. Phys. C6, L139 (1973).

19. R. Georges, Acad. Sci. (Paris) 268B 16 (1969).

20. P. Raghavan, R. S. Raghavan, and W. B. Holzapfel, Phys. Rev. Lett. 28, 903 (1972).

FIGURE CAPTIONS

Fig. 1. Crystallographic and Magnetic Structure of $KNiF_3$ and K_2NiF_4.

Fig. 2. Reduced Temperature/Hyperfine Field Plot for Cd-doped MnF_2 and $RbMnF_3$.

Fig. 3. Time Spectrum of Cd-doped MnS at 1 bar and 20 kbar. The solid line is a least squares fit to a pure magnetic interaction in polycrystalline material. The time calibration is 0.888 ns/channel.

B. Paramagnetic Shifts and Spin-Flop in Supertransferred Hyperfine Structure of ^{111m}Cd in $RbMnF_3$

Recently [1] we reported the PAC of ^{111m}Cd doped as a substitutional impurity into the antiferromagnetic perovskites $RbMnF_3$, $KCoF_3$ and $KNiF_3$. The hyperfine field at the Cd nucleus is caused by unpaired spin density in outer (4s,5s) Cd s-orbitals, transferred from the six nearest magnetic neighbors along linear Mn^{2+} - F^- - Cd^{2+} bonds. Since the contact field produced by an s electron is opposite to its spin, the hyperfine field at the Cd nucleus should be parallel to the magnetic moment of the six nearest transition metal ions. In the antiferromagnetic state only the magnitude of the supertransferred hyperfine interaction is obtained, but the sign can be measured in the paramagnetic state by applying an external magnetic field.

In this Letter we report the time differential PAC of ^{111m}Cd doped into paramagnetic, polycrystalline $RbMnF_3$. The spectra (Fig. 1) were observed at 300°K and 87°K (close to the Néel point T_n = 83°K), with an external field H_{ext} = 31.3 kOe applied perpendicular to the detector axis. In Fig. 1 the perturbation factor [2], $A_{22}G_{22}(t) = A_{22}(0.25 + 0.75 \cos(4\pi\nu_L t)$ is shown for ^{111m}Cd in $RbMnF_3$ and for a diamagnetic standard ($CdCl_2$ solution) in the same external field. The higher frequency of ^{111m}Cd in $RbMnF_3$ corresponds to a higher effective field $H_{eff} = H_{ext} + \Delta H$. This paramagnetic shift arises from a supertransferred contact field at the Cd nucleus created by polarization of the Mn^{2+} electron spin S = 5/2. Since the electronic spin fluctuations are fast compared to the characteristic time of the PAC experiment, only the effect of the time average

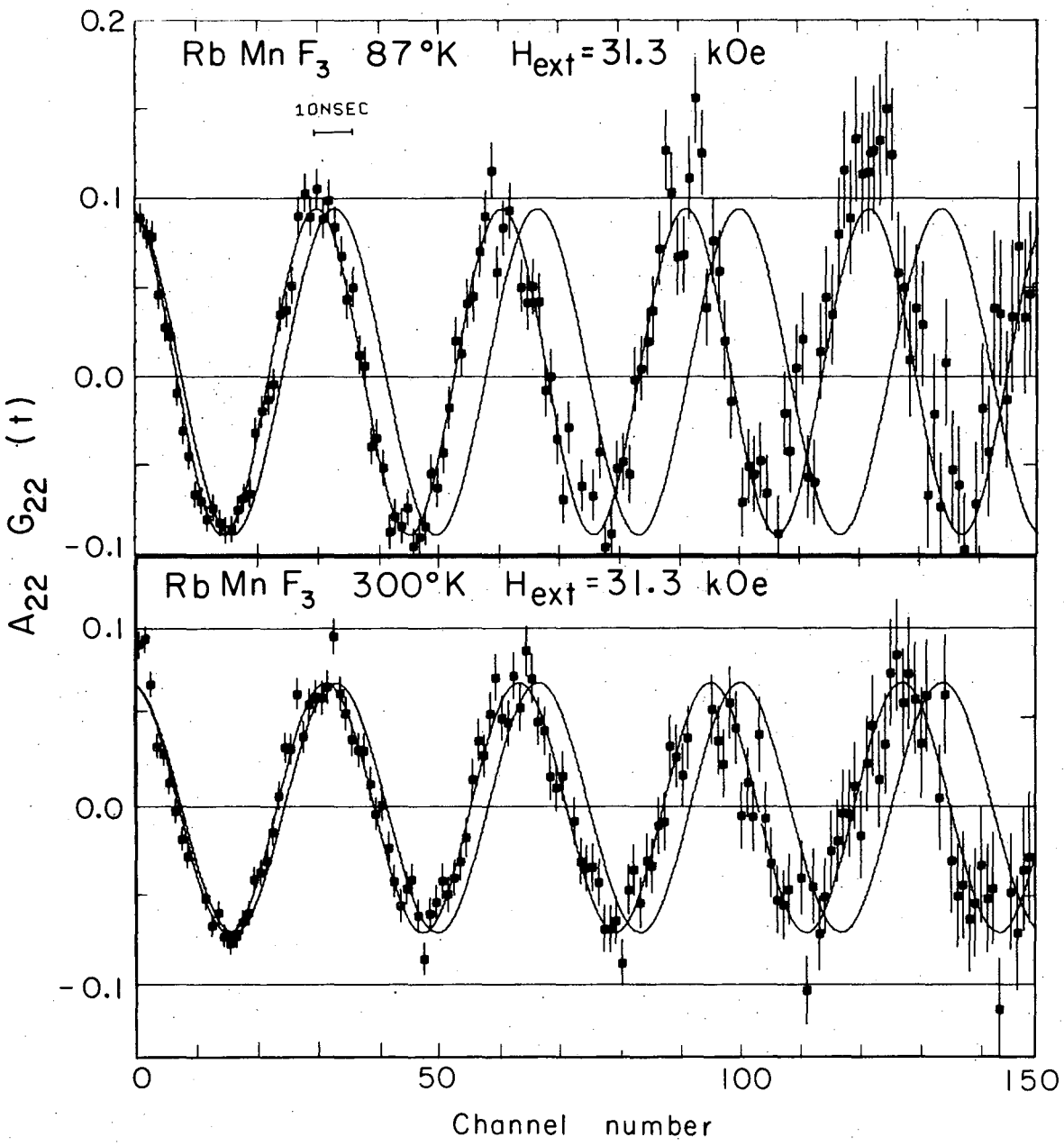
Rb Mn F3 87°K Hext = 31.3 kOe
10NSEC
Rb Mn F3 300°K Hext = 31.3 kOe
A22 G22 (t)
0.2
0.1
0.0
-0.1
0
50
100
150
Channel number
XBL748-3990

Fig. VI-B.1.

$\langle S_z \rangle$ is seen. Therefore, $\Delta H = H_{hf}(4\,^\circ K)\ \langle S_z \rangle / 2.5$, where $H_{hf}(4\,^\circ K)$ = 116 kOe is taken as the low-temperature limit of the hyperfine field at the Cd nucleus in the antiferromagnetic state and $\langle S_z \rangle = 5/2$ has been used as the local value of $\langle S_z \rangle$ for T = 4 °K. (A small zero-point spin deviation has been neglected in this estimate). The spin expectation value $\langle S_z \rangle = (-\chi_m H_{ext})/g\beta N_L)$ in the paramagnetic state can be estimated using the molar susceptibility $\chi_m = C/(T+\theta)$. In this way we estimate for ^{111m}Cd in $RbMnF_3$, at 87 °K, ΔH_{est} = +2.0 kOe compared to ΔH_{obs} = + 3.0±0.5 kOe. The lower susceptibility at room temperature corresponds to a smaller paramagnetic shift (Fig. 1). In this way the following relative shifts $\Delta H/H_{ext}$ were observed; $RbMnF_3$: + 9.6±1.6% (87 °K), + 5.1±1.6% (300 °K); $KFeF_3$: + 5.4±2.2% (120 °K); $KCoF_3$: + 4.5±1.6% (120 °K) and $KNiF_3$: + 1.3±1.6% (265 K). Because of the lower susceptibilities, smaller paramagnetic shifts were observed in $KFeF_3$, $KCoF_3$ and $KNiF_3$ compared to $RbMnF_3$/Cd. For $KNiF_3$ the large values of θ and T_N led to a paramagnetic shift that lay within our experimental error. The experiments reported here are analogous to paramagnetic shift measurements that have been made on F nuclei in these lattices, using NMR. Because the Cd field arises from <u>supertransferred</u> hyperfine structure, these shifts provide a stringent test of the proposed mechanism [1] for spin transfer through Mn^{2+} - F^- - Cd^{2+} bonds.

$RbMnF_3$ is a well known antiferromagnet with an exceptionally low critical field H_c = 2.45 kOe for the spin-flop transition. Above this value the spin axis lies perpendicular to the external field. In polycrystalline $RbMnF_3$/Cd (4 °K) the hyperfine fields at the Cd are randomly oriented for H_{ext} = 0, whereas they are confined in a plane perpendicular

to the external field for $H_{ext} > H_c$. Since PAC is sensitive to the orientation of the hyperfine fields relative to the detector axis, this method lends itself to the observation of the spin-flop transition, as shown (Fig. 2). The time spectra were taken with the detectors at 180° parallel to H_{ext}. In this case the perturbation factor can be written as $A_{22}G_{22}(t) = A_{22}(1-b_1-b_2 + b_1\cos(2\pi\nu_L t) + b_2\cos(4\pi\nu_L t))$. The Fourier coefficients b_1, b_2 are equal for the random distribution $b_1 = b_2 = 0.4$ ($H_{ext} = 0$) and $b_1 = 0$, $b_2 = 0.75$ if the hyperfine fields are in a plane perpendicular to H_{ext}. The spin-flop transition was observed as a change in the ratio b_1/b_2 of the Fourier coefficients (Fig. 2). Since a polycrystalline sample was used, the transition is fairly smeared out; for a precise determination of H_c a single crystal should be used.

This observation gives further microscopic support of both the proposed spin-transfer mechanism and the accepted model for spin-flop transitions.

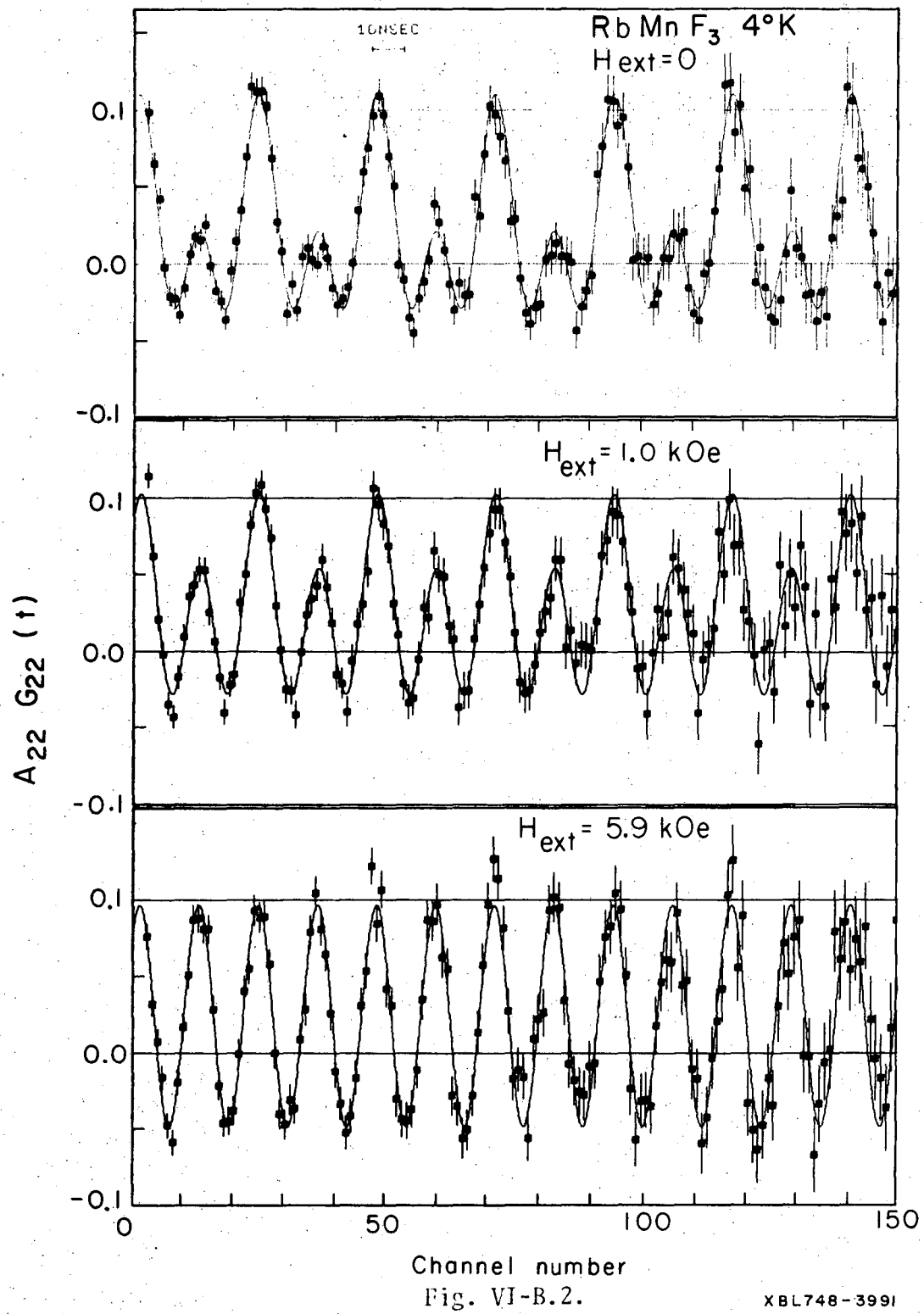

Fig. VI-B.2.

XBL748-3991

REFERENCES

1. H. H. Rinneberg and D. A. Shirley, Phys. Rev. Letters 30 (1973) 1147.

2. H. Frauenfelder and R. M. Steffen, In Alpha-, Beta-, and Gamma-Ray Spectroscopy, ed. by K. Siegbahn (North-Holland, 1965), Vol. 2.

FIGURE CAPTIONS

Fig. 1. PAC of ^{111m}Cd in paramagnetic $RbMnF_3$, compared to a diamagnetic standard ($CdCl_2$ solution) in the same external field H_{ext} = 31.3 kOe.

Fig. 2. Spin-flop transition in $RbMnF_3$ detected by PAC of ^{111m}Cd.

VII. RARE-EARTH VALENCE STATE STUDIES OF THE SERIES RIn_3 AND RSn_3 DERIVED FROM QUADRUPOLE COUPLING CONSTANTS*

A. Introduction

Discussions of the electronic structure of metals usually begin by partitioning the lattice into positively-charged ion cores plus itinerant valence electrons. For many metals this separation is a computational shortcut rather than an experimentally observable feature, but in the rare-earth metals and their compounds the "valence state" has a more exact meaning. The 4f electrons are sufficiently localized to be assigned unambiguously to the ion cores, which then have charges of +3 or sometimes +2. Considerable theoretical and experimental attention has recently been focussed on the question of non-integral rare-earth valence and valence state changes induced by pressure and temperature. Most of the cases studied to date have been rare-earth chalcogenides which have insulating or semi-metallic properties, but potentially interesting metallic cases have also been known for some time.

A study of the susceptibility[1] and lattice constants[1,2,3,4] of the rare-earth series RIn_3 indicated that Yb was in a lower valence state (presumably +2) than the other rare-earths. The large increase in susceptibility[1] noted on cooling to liquid helium temperatures was taken as an indication that the valence of Yb had changed from +2 to +3. In the RSn_3 series $EuSn_3$ and $YbSn_3$ both appear with divalent[4] rare-earths,

*This section of work done in conjunction with D. A. Shirley.

while $CeSn_3$ is trivalent at room temperature and originally appeared to become quadrivalent[4,21] at helium temperatures. The original conclusions concerning the temperature dependence of the rare-earth valencies have been disputed by later Mössbauer[5-8] studies, but a consistent picture for the combined In and Sn series has not been published to date.

The RIn_3 and RSn_3 intermetallics crystallize in the FCC $AuCu_3$ structure, which places the In or Sn at a site with tetragonal symmetry. The non-cubic nature of this site leads to a non-vanishing electric field gradient q which is highly sensitive to changes in the surrounding rare-earth valence state. According to a simple point-charge model, q should scale as Z'/r^3, where Z' is an effective charge. The functional form of this dependence leads to a great sensitivity advantage of field gradients as opposed to lattice constants for determining valence states. A change from +3 to +2 in rare-earth valence might increase the lattice constant by 1-3%, but would reduce q in this simple picture by one-third. We shall show in Section IV that the sensitivity is even greater because q scales as $Z_{RE}-Z_{In,Sn}$ for the $AuCu_3$ structure.

In this paper we report quadrupole coupling constants e^2qQ/h determined by time-differential perturbed angular correlation of the 247-keV state of ^{111}Cd following the electron-capture decay of ^{111}In. Experimental procedures are described in Section B, and results are given in Section C. Our results are interpreted in Section D to show that only $YbIn_3$ contains the rare-earth in the divalent state in the RIn_3 series, while both $YbSn_3$ and $EuSn_3$ contain divalent rare earths at room temperature. Data taken at 4.2°K and in some cases also under 18.5 kbar pressure

indicate that the divalent state appears to be stable in $YbIn_3$ and $YbSn_3$ and that $CeSn_3$ is non-magnetic at liquid helium temperatures with the Ce in the trivalent state.

B. Experimental

The 2.81-day ^{111}In activity, which decays after electron capture via the 173-247 keV cascade of ^{111}Cd, was produced by the $^{109}Ag(\alpha,2n)$ reaction induced by α-particle bombardment of a 0.005 cm natural Ag foil at the Lawrence Berkeley Laboratory 88-Inch Cyclotron. The use of natural Ag (51% Ag^{107}, 49% Ag^{109}) necessitated waiting about 36 hours for the In^{109} (4.3 hr) to decay away, after which the In and Ag were separated using magnesium hydroxide precipitation at a pH of 8-9. Generally .1-.2 mg of In carrier was added, and the activity plated out of a formate-buffered sulfate solution (pH 2) onto an In or Sn foil.

The active foil and stoichiometric amounts of rare-earth metals were then arc-melted under argon on a water cooled Cu hearth. Because the components for $YbIn_3$, $YbSn_3$, and $EuSn_3$ reacted vigorously during melting, some caution was required to produce these compounds without splattering and loss of material. An additional check we also made these compounds by encapsulating the pure metals in a tantalum cruicible and sealing under argon in a quartz tube prior to oven heating. Samples made by these two methods yielded identical coupling constants within experimental error.

Efforts to prepare $EuIn_3$ failed. This is consistent with references 2 and 9 which indicated that only EuIn, $EuIn_2$, and $EuIn_4$ form stable

intermetallics. The attempt to make $EuIn_3$ resulted in a spectrum which was identical to that of $EuIn_4$ when the latter compound was made stoichiometrically. The heavy RSn_3 compounds from Tb to Lu (with the exception of $YbSn_3$) cannot be made in the FCC phase in an arc-furnace or oven at conventional pressures. Our samples of $GdSn_3$ also showed evidence for not being single phase, but there was no difficulty in extracting the quadrupole coupling constant to ±10%.

The time spectra were recorded on four 3.8×5.1 cm NaI(Tl) scintillation crystals mounted on 56 DVP photomultipliers using conventional fast-slow logic. The detectors were arranged in a square array, labeled cyclically A,B,C,D. Two 180° (AC and BD) and two 90° (BC and AD) coincidence spectra were routed to a Scipp 1600 channel pulse-height analyzer and later dumped onto magnetic tape for subsequent analysis. The time resolution measured with a ^{22}Na source with the energy windows set at 173 and 247 keV was 2.0 ns FWHM. The time-to-amplitude converter (Ortec 437) was calibrated using an Eldorado 610 digital delay generator.

When four detectors are used in this way, with A and B the "start" detectors (recording the 173-keV photons) and with C and D the "stop" detectors (247-keV photons), the time-modulation function $\bar{Q}_{22}A_{22}G_{22}(t)$ can readily be extracted[10] from the four coincidence counting rates

$$W_{AC}(\theta,t) = N_o\, e^{-t/\tau_N}\, \varepsilon_{AC}[1 + Q_{22}(AC)A_{22}G_{22}(t)P_2(\cos\theta_{AC})],$$

etc., by forming the ratio

$$-\frac{2}{3}\left\{\left[\frac{W_{AC}}{W_{AD}}\frac{W_{BD}}{W_{BC}}\right]^{1/2} - 1\right\} \cong Q_{22}A_{22}G_{22}(t) = A'_{22}G_{22}(t).$$

This eliminates the total counting rate N_o, the nuclear lifetime τ_N, and to a good approximation the coincidence efficiencies ε_{AC}, etc. Only an average solid-angle correction factor $\overline{Q}_{22} \cong 0.9$ remains. For convenience it is absorbed into the "effective" angular correlation coefficient A'_{22}.

C. Results

The In and Sn sites in these compounds have tetragonal symmetry. They can therefore be treated as cases of randomly-oriented, axially-symmetric electric field gradients. The perturbation factor for this case, with I = 5/2, has the analytic form[11]

$$(1) \quad G_{22}(t) = 1/5 + (13/35)\cos \omega_o t + (2/7)\cos 2\omega_o t + (1/7)\cos 3\omega_o t.$$

Here ω_o is a basic frequency given by

$$(2) \quad \omega_o = 3\, e^2qQ/20\hbar .$$

Figures 1 and 2 show the time modulation of typical $A'_{22}G_{22}(t)$ functions due to the precession of the quadrupole moment of the 247-keV level of ^{111}Cd in the electric field gradient present at the In and Sn sites. The solid curve is a least-squares fit to Eq. 1. The fit yields the basic radial modulation frequency ω_o where q is the electric field gradient for Cd at the In site and Q is the quadrupole moment of the 247-keV ^{111}Cd level. In Table I we have listed the lattice constants as well as the quadrupole coupling constant e^2qQ/h (MHz), derived using Eq. (2).

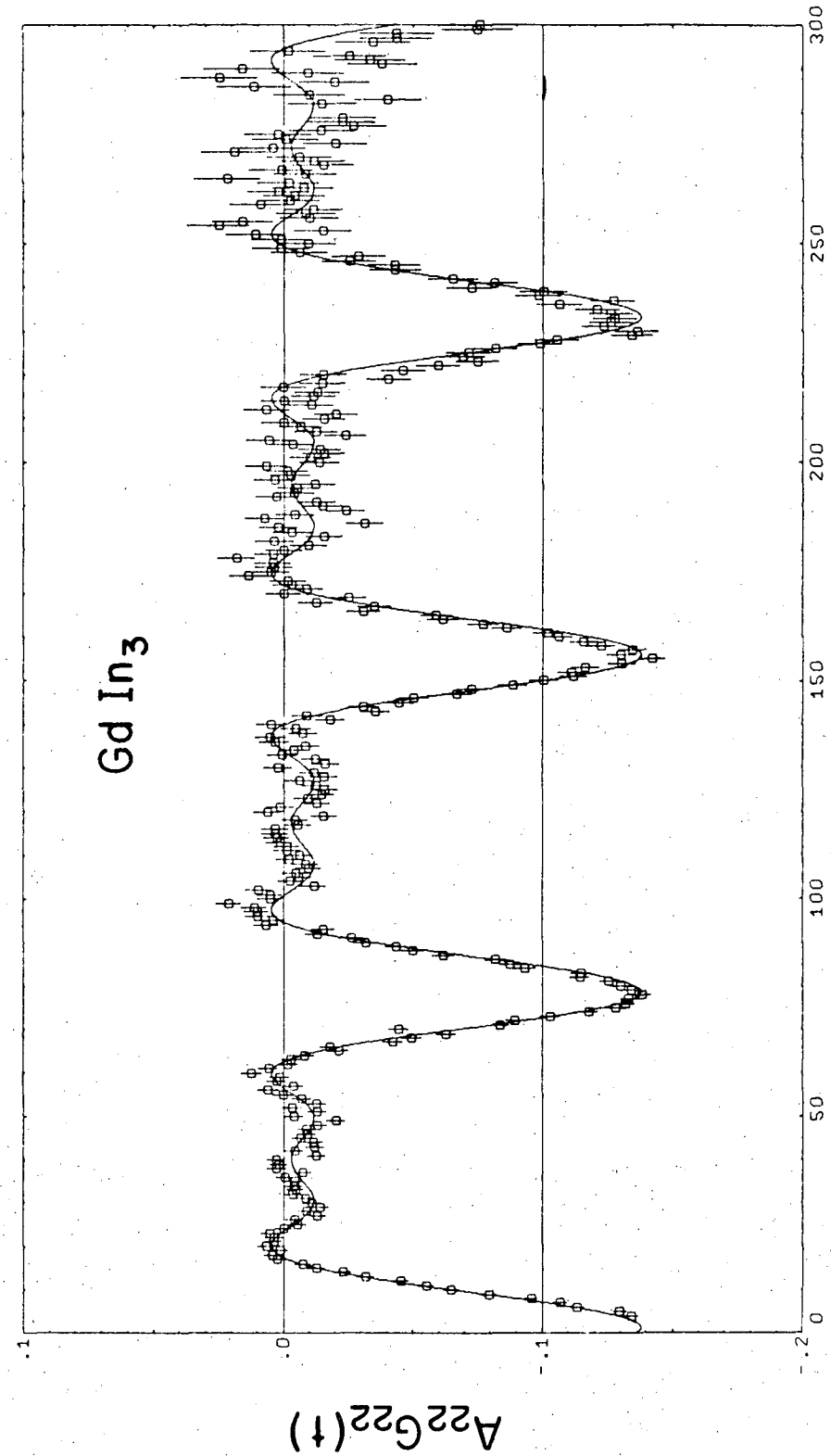

XBL 758-3706

Fig. VII-1.

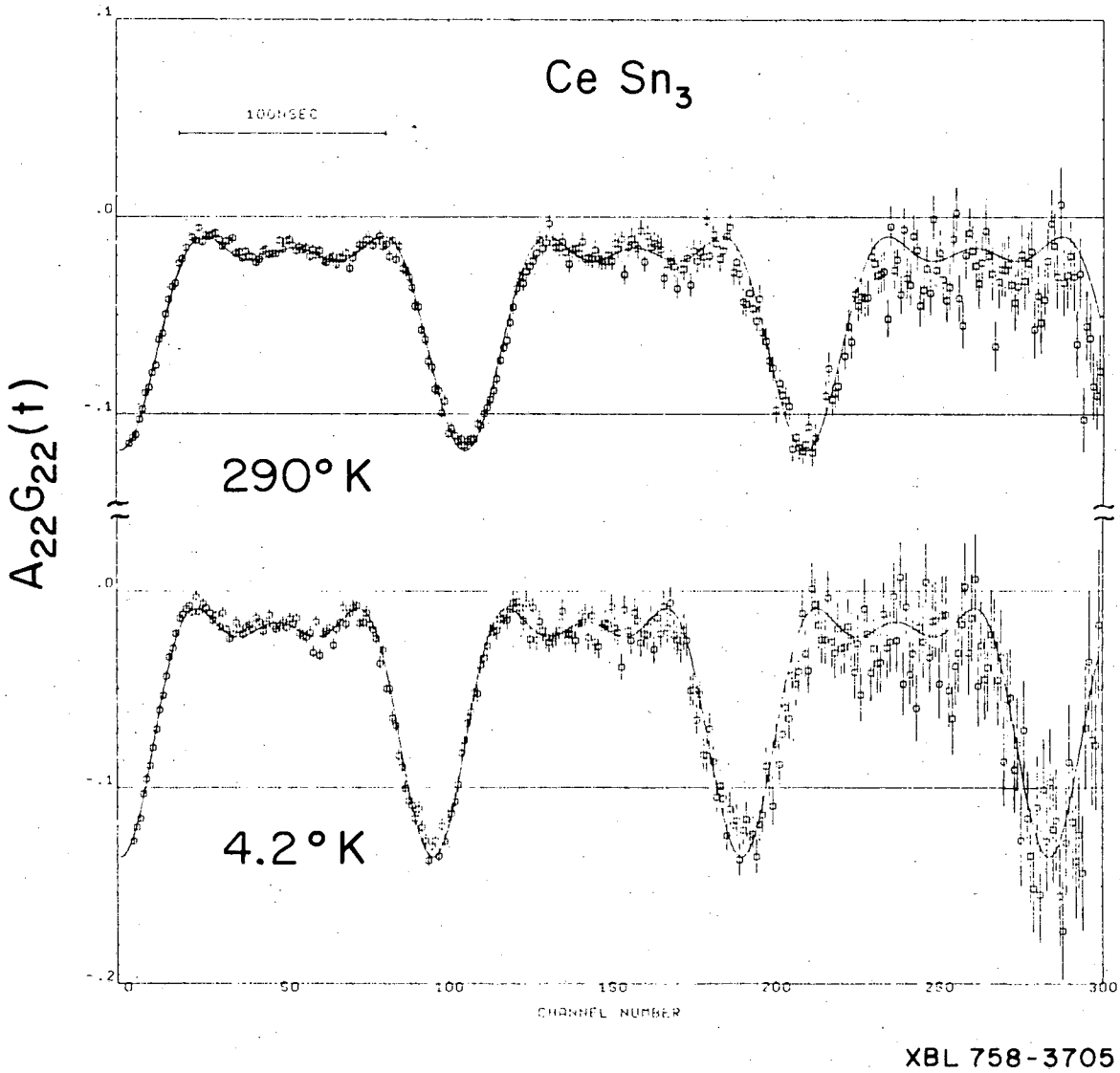
Ce Sn3
100NSEC
290° K
4.2° K
A22G22(t)
.1
.0
-.1
-.2
0
50
100
150
200
250
300
CHANNEL NUMBER
XBL 758-3705

Fig. VII.2.

Table I.A

Compound		Lattice constant[a] (KX)*	$\lvert e^2qQ/h \rvert$ (MHz)
$LaIn_3$		4.7250	72.5±1.1
$CeIn_3$		4.6798	77.9±1.2
$PrIn_3$		4.6622	78.5±1.2
$NdIn_3$		4.6460	80.0±1.2
$SnIn_3$		4.6166	81.4±1.2
$GdIn_3$		4.5973	84.2±1.3
$TbIn_3$		4.5804	86.2±1.3
$DyIn_3$		4.5699	86.4±1.3
$HoIn_3$		4.5640	86.7±1.3
$ErIn_3$		4.5552	87.7±1.3
$TmIn_3$		4.5492	87.7±1.3
$YbIn_3$	(RT)	4.6053	38.7±0.8
	(4.2° K)	---	43.4±0.9
	(RT, 18.5 kbar)	---	45.0±1.4
$LuIn_3$		4.5434	86.7±1.3

a. Ref. 4.

* KX = 1.002495 Å, as cast, RT.

Table I.B

Compound		Lattice constant[a] (KX)*	$\lvert e^2qQ/h \rvert$ (MHz)
$LaSn_3$	(RT)	4.7598	33.9±1.0
	(4.2° K)	---	35.0±1.1
$CeSn_3$	(RT)	4.7119	39.8±1.2
	(RT, 18.5 kbar)		43.7±1.3
	(4.2° K)		43.8±1.3
	(4.2° K, 18.5 kbar)		47.0±1.4
$PrSn_3$		4.7064	41.5±1.2
$NdSn_3$		4.6965	41.4±1.2
$SmSn_3$		4.6772	42.6±1.3
$EuSn_3$		4.7349	12.7±1.3
$GdSn_3$		4.6681	42-43±4.3
$YbSn_3$	(RT)	4.6720	21.9±1.1
	(4.2° K)		25.6±1.3
	(4.2° K), 18.5 kbar)		29.7±1.8

a. Ref. 4.

* KX = 1.002495 Å, as cast, RT

D. Interpretation

Recent theoretical discussions[12-16] have highlighted the difficulties of calculating the valence electron contribution to the electric field gradients (EFG) of metals and alloys when the exact charge distribution around the atoms is not known. The essential difficulty arises because the charge distribution of the itinerant valence electrons is actually largely centered around the ion cores, where it tends to shield the ionic core contribution to q, and can result in either the core or valence electrons dominating and determining the sign of q. Even the separation of the EFG into separate independent core and electron contributions has been brought into question by a recent study[17] of the systematics of experimental data on metal and alloy gradients which indicates an apparent scaling of the electron contribution to the total ionic core term $eq_{lat}(1-\gamma_\infty)$.

We will not attempt a quantitative interpretation of the magnitude of e^2qQ/h, which would require a rather elaborate calculation of dubious value in light of the present understanding of the contributions to electric field gradients in metals and alloys. Instead we will adopt the form

$$eq = eq_{lat}\ (1 - \gamma_\infty)(1 + F_e) \qquad (3)$$

suggested by Ref. 18 and empirically justified on a systematic basis by Raghavan et. al.[17] In Eq. 1 eq_{lat} is the point charge contribution of the "ionic" cores, γ_∞ the Sternheimer factor, and F_e a term which reflects the valence electron contribution.

Using the method of plane-wise summation[19] for a lattice of infinite extent, de Wette and Schacher[20] performed the lattice sum calculation for the FCC structure at the In or Sn site. The result of their calculation yields

$$eq_{lat}(In,Sn) = -e(8.67)(Z_{RE}-Z_{In,Sn})/a_o^3, \qquad (4)$$

where Z_{RE} and $Z_{In,Sn}$ are the assumed metal valencies and a_o is the lattice constant. The factor 8.67 for the infinite lattice can be compared to the number 7.0, which we calculated assuming only interactions out to the third nearest neighbor. Most of the contribution to the EFG is thus short-range in nature. The quadrupole coupling constants of Table I are related to Eq. 3 by

$$|e^2qQ/h| = |e^2Q(8.67)(Z_{RE}-Z_{In,Sn})(1-\gamma_\infty)(1+F_e)/ha_o^3|. \qquad (5)$$

The study of the rare earth valence and its possible fluctuations are contained in the form of Eq. 5. If the rare earths in the series RIn_3 or RSn_3 were all in the +3 valence state and the electronic screening was constant, then a plot of e^2qQ/h vs Z'/a_o^3 would be roughly constant. Any slow variation in screening throughout the series should be reflected in q, while a different valence state should appear as an abrupt change. To factor out the a_o^{-3} effect due to the gradual variation in lattice constants, we have plotted $(a_o^3)(e^2qQ/h)$ vs atomic number. Figures 3 and 4 show the data for the RIn_3 and RSn_3 compounds with $AuCu_3$ structure as well as the lattice constants of Ref. 4. The near constancy of $(a_o^3)(e^2qQ/h)$ throughout the series argues strongly for the rare earth ions being in the same valence state-presumably +3- and for the screening effect of the valence

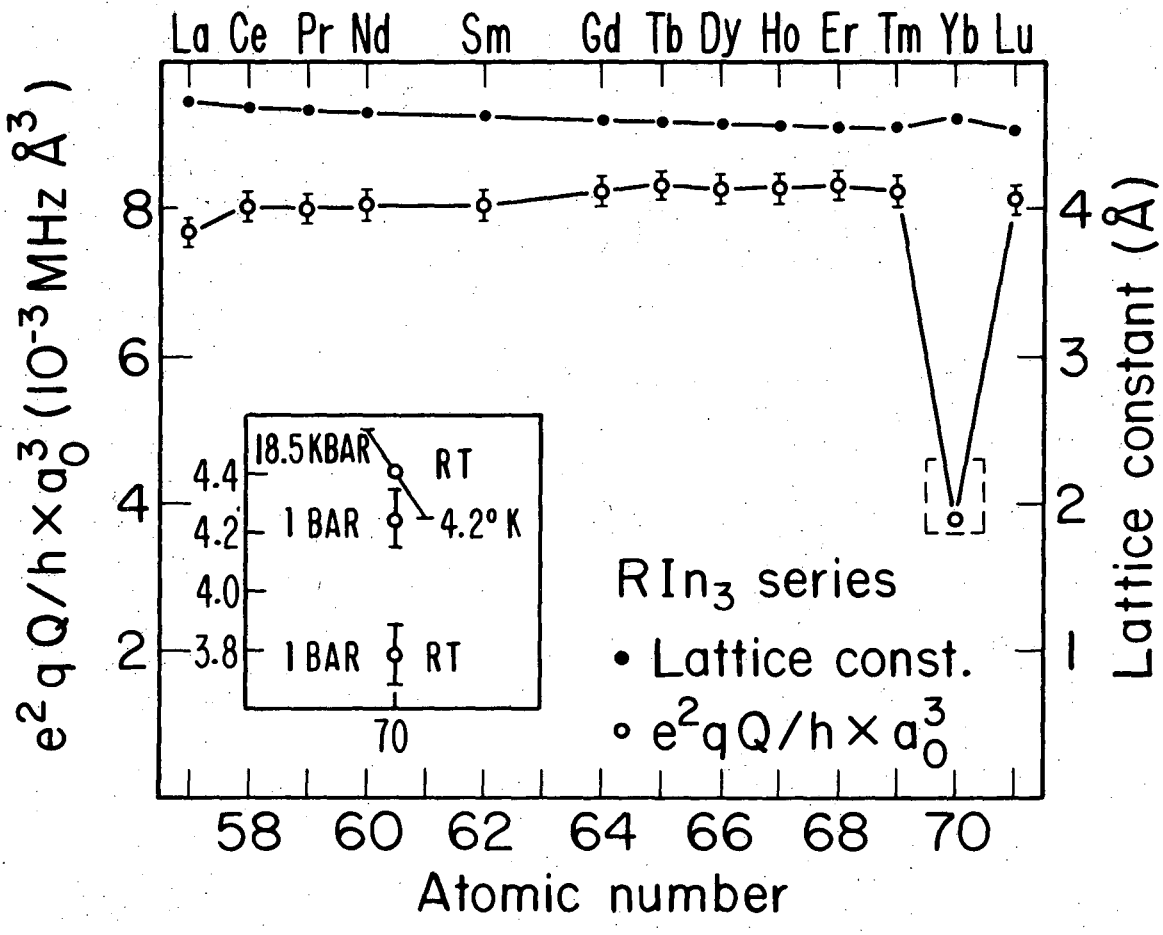

Fig. VII-3.

XBL758-3708

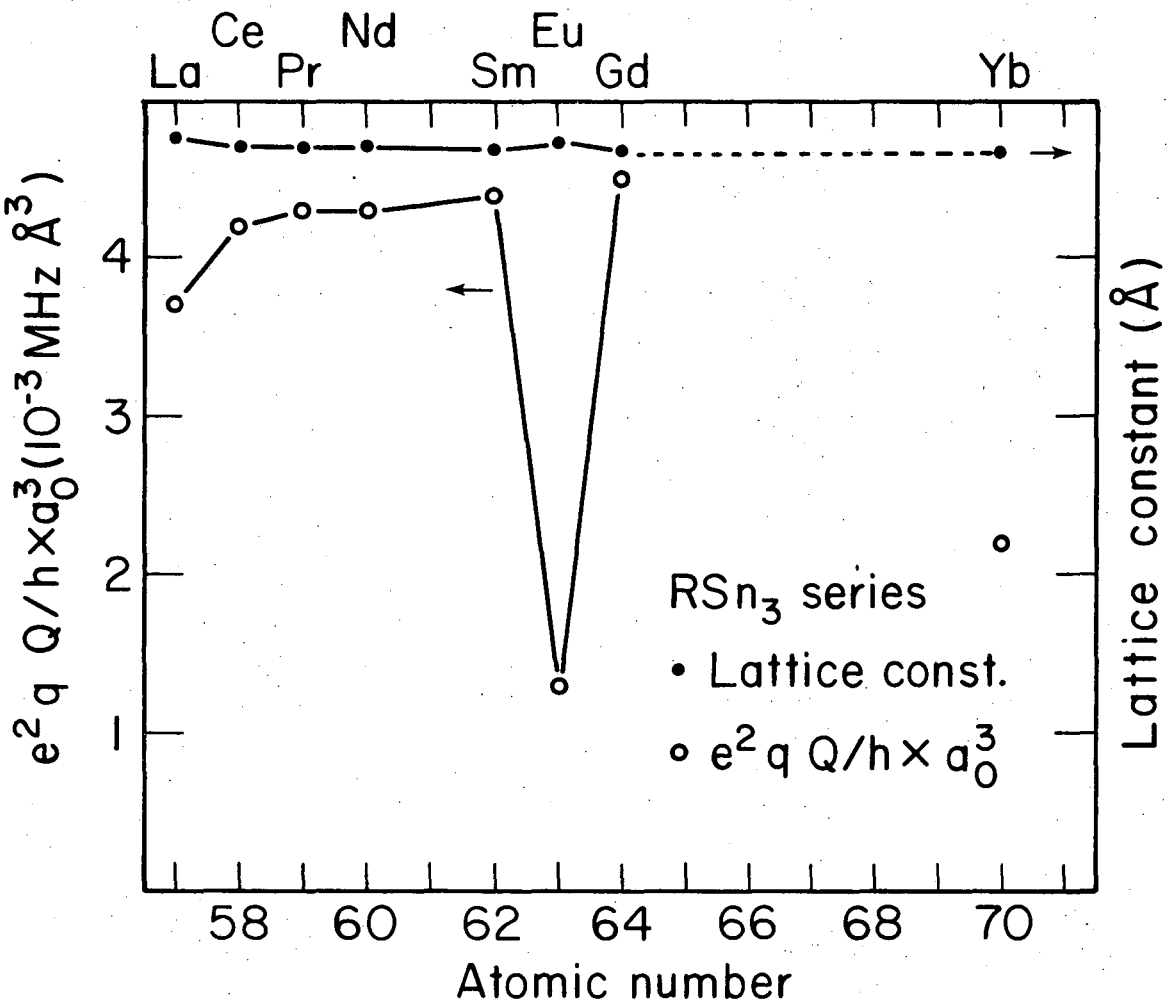

Fig. VII-4. XBL758-3704

electrons being essentially the same across the rare earth row in these compounds. Dramatic drops are seen to occur at $YbIn_3$, $EuSn_3$, and $YbSn_3$. The lattice constant variations for these three compounds from the +3 line are of the order 1-2%, and clearly cannot account for the magnitude of the reductions. The percentage deviation in the quadrupole coupling constants is ~ 30-50 times larger than that noted in the lattice constants, confirming the great sensitivity of this parameter to the rare-earth valence state.

Room temperature susceptibilities,[1,21] lattice constants,[1-4] and Mössbauer spectra[5-8] are all consistent with the assignment of the divalent state to the rare earth in these three compounds at room temperature. Gschneidner[22] has also thermodynamically evaluated heat of formation data for a number of Yb and Eu compounds and has estimated that for Yb or Eu to be trivalent in a particular compound requires the heats of formation for the trivalent lanthanides to be more negative than roughly -9 and -23 kcal/gm- at of rare earth respectively. One thus generally expects Yb and especially Eu to be divalent in all but the most ionic or covalent compounds.

We would like to show that the assignment of di- and trivalent states is also consistent with the absolute magnitudes of the quadrupole coupling constants. Equation 5 requires the lattice constants, and we will adopt the value a_o = 4.65 Å for the purpose of estimating the coupling constants. The error in using an average lattice constant is less than the uncertainty in the quadrupole moment Q of the I = 5/2 intermediate state, whose literature values span a factor of three. We will use the value Q = 0.44b[18] and the Sternheimer factor for Cd^{2+} calculated by Feiock and Johnson[23] γ_∞=-29.27.

The choice of the charges at the In and Sn sites is dictated by several considerations. In the RIn_3 series the assignment of +3 for In and +3 for the rare earths (except for Yb) would cause the electric field gradient to vanish identically. This is not an artifact of performing a finite lattice sum but is a rigorous symmetry argument for an FCC lattice in which all sites are equivalently charged. From Mössbauer measurements in $EuSn_3$, Loewenhaupt and Hüfner[8] assign Sn as divalent rather than tetravalent. This pulling of change toward In or Sn is consistent with the electronegativities tabulated by Teatum[21] et al., who assign values around 1.2 to the rare earths and 1.4-1.6 for In and Sn. Finally one requires that the order of magnitude of the coupling constants should be predicted reasonably regardless of whether the rare earths are di- or trivalent. If one assigns +3 to the rare earths, then a +1 valence at In and +2 at Sn is consistent with these considerations. We will also take $|(1+F_e)| \approx 1$ which is consistent with the observations of Ref. 17 that F_e has values of order -2 to -3. It would be perhaps more realistic to take $|Q(1+F_e)| \approx 0.5$ since the uncertainty in Q is so large. The assignment of +1 to In and +2 to Sn deserves an additional comment. These valence assignments would imply neutral $Cd(4d^{10}5s^2)$ rather than Cd^{2+} $(4d^{10})$ with the associated change in Sternheimer factor. One can estimate this effect by looking at the configurations for I in +7 $(4d^{10})$ and +5 $(4d^{10}5s^2)$ valence states, for which the Sternheimer factors[23] are $\gamma_\infty(I^{+7}) = -16.84$ and $\gamma_\infty(I^{+5}) = -18.24$. This effect is of order 10%, yielding $\gamma_\infty(Cd^o) \sim -32$, and can be incorporated into $|Q(1-\gamma_\infty)(1 + Fe)|$. For $Q \simeq 0.44$ barns, $1 - \gamma_\infty \simeq -33$ and $|1+F_e| \sim 1$, we obtain $|Q(1-\gamma_\infty)(1+F_2)|$ ~ 14.5, with a large uncertainty. Using this estimate and $a_o = 4.65$ Å, we obtain

$$|e^2qQ/h| \simeq 44(Z_{RE} - Z_{In,Sn}) \text{ MHz}.$$

Considering first the RIn_3 compounds with $Z_{RE} = +3$ and $Z_{In} = +1$, we expect a coupling constant of order 88 MHz. Most of the experimental values are between 80 and 90 MHz. The agreement is certainly fortuitous in view of the uncertainties in Q, F_e, and the valence assignment of +1 for In. However, a rather consistent picture follows from these assignments. For $YbIn_3$ with a divalent rare earth, one expects a 50% reduction to 44 MHz. The measured value is 38.7 MHz. In addition, one expects that if Sn is divalent the Sn series with <u>trivalent</u> rare earths should be around 44 MHz, and the experimental values generally fall between 40-45 MHz. For $Z_{Sn} = +2$ however, the divalent rare earths $EuSn_3$ and $YbSn_3$ should have coupling constants equal to zero by symmetry. The $EuSn_3$ value has dropped to 12.7 MHz, while $YbSn_3$ is higher at 21.9 MHz. The failure of these values to vanish identically points out the deficiency of expecting more than qualitative agreement with our estimates of the coupling constants.

As an additional check we measured $BaSn_3$, in which one expects the stability of the Xe core to insure Ba being divalent, and found a coupling constant of approximately 19 MHz. The purpose of the estimate was not to justify a point charge model or our assignment of the charges to the rare earths, In, and Sn, but rather to emphasize that a rather simple picture of the field gradient can yield useful insight into the qualitative trends in these alloys.

We now examine the question of the temperature and pressure dependence of valence fluctuations in these alloys. Susceptibility[1,21] data, thermal expansion measurements,[4] and lattice constants [4] had indicated

that $YbIn_3$ and $CeSn_3$ appeared to become trivalent and partially tetravalent respectively on cooling to 4.2° K and that $YbSn_3$ might exist in a mixed valence state at room temperature. We have measured all of these compounds at 4.2° K and find shifts of order 10-15%, which are not nearly large enough to be representative of a complete change in valence state. We feel that most of the shift can be accounted for by the thermal contraction of the lattice. Figure 2 also shows that $CeSn_3$ is non-magnetic. in accord with earlier Mössbauer[5] data. It is interesting to note that $YbSn_3$ probably undergoes a lattice distortion on cooling to liquid helium temperatures, because the PAC pattern is clearly distorted from that expected for axial symmetry. We have checked this to see if it was an artifact of the sample preparation and have found it to be a reproducible feature of the low temperature spectra. Room temperature spectra show no such distortion.

$YbIn_3$(RT), $YbSn_3$(4.2 K), and $CeSn_3$(RT and 4.2 K) were also run in a clamping type pressure cell to 18.5 kbar in order to see if we could induce a valency fluctuation. Shifts on the order of those associated with cooling to helium temperatures were observed, but in no case did we observe an increase which would put the points on the "trivalent line" of Figs. 3 and 4. We conclude that the compounds $CsSn_3$, $YbSn_3$, and $YbIn_3$ show no evidence for a bulk valence instability down to liquid helium temperatures and pressures to 18.5 kbar. Previous Mössbauer data on $CeSn_3$[5] and $YbSn_3$[7] have come to similar conclusions.

In summary we have systematically studied the RIn_3 and RSn_3 compounds with $AuCu_3$ structure using TDPAC and have demonstrated the high

sensitivity of this technique to the rare earth valence state. We have also conducted experiments to probe the possible temperature and pressure dependence of the rare earth valence in $CeSn_3$, $YbSn_3$, and $YbIn_3$ and find no evidence for bulk valence fluctuations in these compounds.

ACKNOWLEDGMENTS

One of us (GPS) wishes to thank Ruth Mary Larimer and Harry Harrington for assistance with the 88-Inch Cyclotron target and Wini Heppler and Gerda Bolz for help in working up the activity and sample preparation.

REFERENCES

1. K. H. J. Buschow, H. W. De Wijn, and A. M. Van Diepen J. Chem. Phys. 50(1) 137 (1969).
2. Yu. B. Kuz'ma and V. Ya., Markiv Kristallografiya 9(2) 279 (1964).
3. J. L. Moriarity, J. E. Humphreys, R. O. Gordon, and N. C. Baenziger Acta Crystallog. 21(5), 840 (1966).
4. I. R. Harris and G. V. Raynor, J. Less Common Metals 9, 7 (1965).
5. G. K. Shenoy, B. D. Dunlap, and G. M. Kalvius, J. Appl. Phys. 41, 1317 (1970).
6. F. Borsa, R. G. Barnes, and R. A. Reese, Phys. Stat. Sol. 19, 359 (1967).
7. A. Percheron-Guegan, J.-C. Achard, O. Gorochou, F. Gonzalez-Jimenez, and P. Imbert, J. Less Common Metals 37, 1 (1974).
8. M. Loewenhaupt and S. Hüfner, Physics Letters 30A, 309 (1969).
9. W. Koester and J. Meixner, Z. Metallk. 56, 695 (1965).
10. B. Erik Karlsson, Arkiv. Fysik 22, 1 (1962).
11. R. M. Steffen and H. Frauenfelder, Perturbed Angular Correlations, ed. E. Karlsson, E. Matthias, and K. Siegbahn (North Holland, 1964).
12. R. E. Watson, A. C. Gossard, and Y. Yafet, Phys. Rev. 140, A375 (1965).
13. N. C. Mohapatra, C. M. Singal, and T. P. Das, Phys. Rev. Lett. 31, 530 (1973).
14. N. C. Mohapatra, C. M. Singal, T. P. Das, and P. Jena, Phys. Rev. Lett. 29, 456 (1972).

15. K. W. Lodge and C. A. Scholl, J. Phys. F: Metal Phys. 4, 2073 (1974).

16. K. C. Das and D. K. Ray, Phys. Rev. 187, 777 (1969).

17. R. S. Raghavan, E. N. Kaufmann, and P. Raghavan, Phys. Rev. Lett. 34, 1280 (1975).

18. E. Bodenstedt, U. Ortabasi, and W. H. Ellis, Phys. Rev. B 6, 2909 (1972).

19. F. W. De Wette, Phys. Rev. 123, 103 (1961).

20. F. W. De Wette and G. E. Schacher, Phys. Rev. 137, A92 (1965).

21. T. Tsuchida and W. E. Wallace, J. Chem. Phys. 43, 3811 (1965),

22. K. A. Gschneidner, Jr., J. Less-Common Metals 17, 1 (1969).

23. F. D. Feiock and W. R. Johnson, Phys. Rev. 187, 39 (1969).

24. E. Teatum, K. Gschneidner, Jr., and J. Waber, LA-2345 (1960).

FIGURE CAPTIONS

Figure 1. Experimental and least squares fit (solid line) time modulation spectrum for ^{111}In in $GdIn_3$. The time calibration is 1.03 ns/channel.

Figure 2. Experimental and least squares fit (solid line) time modulation spectra of ^{111}In in $CeSn_3$ at 290 and 4.2° K. The time calibration is 1.62 ns/channel.

Figure 3. Lattice constants and quadrupole coupling data for RIn_3 compounds plotted against atomic number.

Figure 4. Lattice constants and quadrupole coupling data for RSn_3 compounds plotted against atomic number.

TECHNICAL INFORMATION DIVISION
LAWRENCE BERKELEY LABORATORY
UNIVERSITY OF CALIFORNIA
BERKELEY, CALIFORNIA 94720